Optimization of laser-induced graphene membrane for simultaneous photo- and electro-thermal membrane distillation

Journal of Membrane Science 705 (2024) 122900

Contents lists available at ScienceDirect

Journal of Membrane Science

journal homepage: www.elsevier.com/locate/memsci

Optimization of laser-induced graphene membrane for simultaneous photo- and electro-thermal membrane distillation

Yong Zen Tan [a,1], Navin Raj Tamilselvam [a], Nur Hashimah Alias [a,c,1], Jia Zheng Oor [a,b], Ronn Goei [d], Alfred Iing Yoong Tok [d], Jia Wei Chew [a,b,e,*]

[a] School of Chemistry, Chemical Engineering and Biotechnology, Nanyang Technological University, 637459, Singapore
[b] Singapore Membrane Technology Center, Nanyang Technological University, 637141, Singapore
[c] Department of Oil and Gas Engineering, School of Chemical Engineering, College of Engineering, Universiti Teknologi MARA, 40450, Shah Alam, Selangor, Malaysia
[d] School of Materials Science and Engineering, Nanyang Technological University, 50 Nanyang Avenue, 639798, Singapore
[e] Chemical Engineering, Chalmers University of Technology, 412 96, Gothenburg, Sweden

ARTICLE INFO

Keywords:
Membrane distillation
Laser-induced graphene
Silver nanoparticles
Surface modification
Localized heating
Plasmon resonance

ABSTRACT

To optimize the Laser-Induced Graphene (LIG) Janus membrane, this study investigated the effects of membrane pore structure, polydimethylsiloxane (PDMS) coating sequence and addition of silver (Ag) nanoparticles on membrane distillation (MD) performance. This study aimed to enhance the photothermal characteristics of graphene while using the intrinsic electrical conductivity for simultaneous photo- and electrothermal MD. Operating at the same photo- and electro-thermal power input, the LIG Janus membrane made by treating the membrane face with smaller pores (i.e., shiny side) gave an improved flux performance of up to 53.6% and a decrease in specific energy of 35.4% compared to that by treating the membrane face with larger pores (i.e., dull side). The effect of the PDMS coating sequence also depended on the pore structure. For the face with smaller pore structures, coating PDMS before laser irradiation (PDMS-BLSS) gave a flux improvement of up to 24.5% and a decrease in specific energy of 19.7%, compared to coating PDMS after laser irradiation (PDMS-ALSS). As for the face with larger pore structures, coating PDMS before laser irradiation (PDMS-BLDS) resulted in a flux reduction of up to 20.8% and an increase in specific energy of 27.1%, compared to coating PDMS after irradiation (PDMS-ALDS). The LIG Janus membranes embedded with Ag nanoparticles led to improved photothermal heating properties, improving flux by 43.1–65.8% and decreasing specific energy by 15.2–30.5% while maintaining similar electrothermal heating properties. Carrying out simultaneous photo- and electro-thermal MD indicates that only the Ag-doped Janus LIG membrane gave a synergistic effect whereby the flux of the combined heating mode was higher than the summation of the fluxes obtained when operating in the individual heating modes.

1. Introduction

At present, desalination technology has enabled us to satisfy the growing demand for access to freshwater resources by treating seawater and/or brackish water. Reverse osmosis (RO) has gained widespread industrial adoption primarily due to its low specific energy consumption (SEC); i.e., the amount of energy needed to produce a specific volume of water). Currently, medium to large-sized RO plants have achieved significant reductions in SEC, with values ranging from 2.5 to 7 kW h/m^3 [1–3]. This represents a notable advancement in energy efficiency, making RO an increasingly attractive and viable solution for water treatment. Nonetheless, RO requires the utilization of high-grade energy in the form of electricity, which results in significant energy destruction despite its low SEC values [3]. Another environmental issue of concern is that the RO process globally produces 141.5 million m^3 of brine daily [4]. Sudden drastic fluctuations in seawater salinity have the potential to negatively impact marine ecosystems in terms of the growth rates and development of larvae. In contrast, the high salinity of brine diminishes the dissolved oxygen in seawater, leading to the risk of hypoxia in marine organisms, especially seagrasses and microorganisms such as benthic heterotrophic bacteria and zooplankton [5–10].

In particular, benthic heterotrophic bacteria play a crucial role in regulating diverse biochemical processes such as nutrient remineralization and organic matter decomposition in the upper sediment layers,

* Corresponding author.
[1] These authors contributed equally to this work.

https://doi.org/10.1016/j.memsci.2024.122900
Received 8 March 2024; Received in revised form 5 May 2024; Accepted 15 May 2024
Available online 16 May 2024

which is about a few centimeters. At the same time, the zooplankton serves as the foundation of the marine food pyramid [6,8–10]. According to a recent review conducted by Dhakal et al., RO represents approximately 77 % of the global desalination capacity, which corresponds to around ~88 Mm^3/d [4]. A major challenge for this technology is to lower energy consumption to produce fresh water sustainably [3,11]. As the quest for sustainability becomes an integral part of the world, water purification technologies must also become sustainable. While RO is the dominant process for desalination, it unfortunately leads to highly saline brine waste and demands high-grade energy.

To address this, it is promising to employ MD in conjunction with RO for treating RO brine with the goal of attaining zero liquid discharge, or as a standalone desalination technique that can make use of waste or renewable heat. With the ready availability of alternative heat sources like geothermal energy, solar heat, and industrial waste heat, membrane distillation (MD) has been explored and studied as an emerging technology to reduce the reliance on high-grade energy and mitigate the discharge of saline brine [3,12]. Moreover, instead of discarding and labelling brine as a harmful wasteful byproduct of RO process, brine itself can be further exploited for its valuable fundamental resources, such as lithium, calcium carbonate, and magnesium sulphate, for which the current recovery using existing RO is not efficient. Ideally, RO can be hybridized with a MD crystallizer to achieve zero-liquid discharge (ZLD) while recovering freshwater from seawater. In MD, a hydrophobic membrane with pores typically in the microfiltration range is used to prevent direct flow of liquid water while facilitating the permeation of water vapor through the membrane itself. The water vapor is then captured to be cooled to obtain freshwater as condensate via different methods depending on the configuration [13]. This working principle allows MD to be operated at moderate temperature and low pressure while having a high solute rejection. In contrast to RO, which is a pressure-driven process operating at high pressure, the MD operates at ambient pressure, which minimizes membrane fouling and negates the need for mechanically strong membranes [14]. However, the MD process does not come without disadvantages. Currently, the most significant share of energy consumption in MD is attributed to the heating of the feed. To enhance sustainability, the amount of energy required has to be reduced through various means, for example, (i) the source of energy should be industrial waste heat or renewable green energy such as geothermal and solar heat; (ii) surface or localized heating at the feed-membrane interface can be employed to reduce temperature polarization; and (iii) heat utilization can be improved via photothermal and/or electrothermal heating of the membrane surface. This motivated the current study.

The heat loss across the membrane during filtration reduces the thermal efficiency of the MD process. The combined effect of heat loss and the latent heat of vaporization during water evaporation results in a decrease in the temperature at the interface between the feed and the membrane. As a result, the decrease in the driving force across the membrane hampers the permeation flux in MD. This characteristic is referred to as temperature polarization, whose impact becomes more prominent as the module size of the MD system increases. Consequently, as the process scales up, there is a noticeable decline in the average flux [15]. Enhancing the performance and practical feasibility of MD involves mitigating temperature polarization, specifically addressing the temperature disparity between the feed-membrane interface and the bulk fluid [16].

In recent studies, researchers have focused on localized heating methods, particularly near or on the surface of the membrane itself, to tackle temperature polarization [17,18]. Direct heating of the feed-membrane interface has the potential to reduce the consumption of energy and the cost associated with MD [16,19,20]. Localized heating on the surface of the thin film of fluid at the feed-membrane interface offers greater energy efficiency as compared to preheating the whole bulk feed. In addition to achieving higher flux rates through localized heating, implementing such systems also overcome various challenges associated with heat management, including the prevention of metal corrosion, the reduction of scaling in heat exchangers, and the costs related to thermal loss. There are two methods to carry out surface heating in MD, namely, photothermal heating and electrothermal heating, whereby photothermal heating involves the conversion of light energy to heat energy via absorption or plasmon resonance, while electrothermal heating involves conversion of electrical energy to heat energy via Joule heating. A research gap exists with respect to the effectiveness and efficiency of concurrent application of photothermal and electrothermal localized heating of the feed-membrane interface.

In addition, for a long time, heat generation in noble metal nanoparticles caused by light-to-heat conversion has been considered only as a side-effect. However, light-to-heat generation can be easily achieved by noble metal nanoparticles under laser irradiation, which develops a promising new series of applications in nanotechnology, including the fields of nano-optics, nano thermodynamics, and plasmonic heating. On top of that, silver nanoparticles is one of the great nanoparticles that can generate a heat flux about ten times higher than the one achieved with gold nanoparticles under plasmon resonance conditions [21] and are less expensive than gold [21,22]. Thus, there are various methods available for implementing localized surface heating, including use of an electric heater to directly heat the fluid near the surface of a silver membrane in air gap MD [23], induction heating of the metallic spacers [24,25] or heating the surface of membranes coated with carbon nanotubes [26], utilization of joule heating of membranes surfaces through electrodes physically attached to graphene mixed matrix membrane [27] or membrane surface coated with carbon allotropes [28–30], and photothermal (solar) heating [31,32] (on membranes coated with photothermal materials [28,33–37] or spacers [34,38,39], or mixed within a mixed matrix membranes [40,41]). Among the aforementioned localized surface heating implemented, only one focused on simultaneous photothermal and electrothermal membranes in MD using a CNT composite membrane [28].

Compared to noble metal thermoplasmonics [42], carbon-based materials have attracted considerable attention as photothermal materials, primarily because of their affordability, reusability, and their ability to efficiently convert natural solar light into heat [43–45]. Graphene-based materials show several promising properties within the field of carbon-based photothermal materials, including (i) their enhanced thermal conduction within the plane, which retains heat at the material surface [46,47]; (ii) the naturally occurring defects present in the graphitic lattice, which promotes phonon scattering and thus aids heat capture [48]; and (iii) facilitating the transport of water molecules across the material [49]. It is worth noting that the diverse methods employed in the preparation of graphene structures offer the opportunity to finely adjust the structural characteristics and morphologies, resulting in materials exhibiting broad spectra of optical and photothermal characteristics [50]. Importantly, graphene is electrically conductive, which allows it to be heated up electrothermally via Joule heating.

Conventional solar vaporization systems typically rely on volumetric heating, which involves sizeable thermal masses and substantial heat loss. However, advancements in photothermal materials and interfacial evaporator designs made up of nanostructures allow the evaporation surface to be heated via highly localized photothermal conversion. This allows for maximizing the utilization of solar energy while minimizing thermal dissipation to the surrounding bulk water [17–20]. Recently, the laser-induced graphene (LIG) method attracted immense attention due to its ease of fabrication; low cost; fast single step process [51–55]. However, to date designing and fabricating LIG membranes for membrane distillation applications remains an unsolved challenge because laser irradiation distorts the porous structure of the substrate and limit the performance of the membranes [56]. Thus, exploring a suitable method to fabricate LIG membranes membrane distillation, while maintaining the nanoscale features of the polymeric substrate, is vital to take the LIG application for the membrane to the next step as a great

potential material for water treatment application.

In this study, a series of modifications were conducted on a hydrophilic polyethersulfone (PES) membrane using different protocol sequences to optimize the synthesis of Janus membranes, which comprise a graphene layer with high conductivity and a hydrophobic polydimethylsiloxane (PDMS) surface layer, for simultaneous photo- and electrothermal MD. The series of modifications involved three steps, namely, a silver nanoparticles coating step, a PDMS coating step and a laser-inducted graphitization step. After the modification, the membranes were evaluated utilizing a setup for direct-contact membrane distillation (DCMD), which employed three distinctive localized heating modes (namely, photothermal, electrothermal and combined photo- and electrothermal heating modes). To assess the efficiency of the membranes that have been modified, various parameters were compared across different localized heating modes. The parameters investigated include flux, specific heating energy (Q_{SH}) and single-pass heat utilization efficiency (HUE_{sp}). Moreover, the modified membranes were characterized, including chemical analysis and analysis pore size distribution.

2. Materials and method

2.1. Materials

The commercial polyethersulfone (PES) membrane used in this study was obtained from Millipore Express® PLUS Membrane Filters (refer to Table S1 for specifications). Silver nitrate and ascorbic acid were obtained from Sigma-Aldrich. Meanwhile, polydimethylsiloxane (PDMS) Sylgard 184 was used together with the curing agent (Dow Corning) and (R)-(+)-Limonene (Sigma-Aldrich; a green solvent). Lastly, the sodium chloride (NaCl) was purchased from Merck-Millipore (CAS No. 7647-14-5).

2.2. Coating of silver nanoparticles

For the membranes coated with silver nanoparticles, a single piece of hydrophilic PES membrane (Millipore Express® PLUS Membrane Filters; refer to Table S1 for specifications) was placed with the side to be coated facing up in a 100 mm diameter polytetrafluoroethylene (PTFE) dish, before filling it up with 20 mL of 0.5 wt% of silver nitrate solution. The dish was then placed on an orbital shaker (Standard 3500, VWR) at 50 rpm for 30 min. Then, the membrane was transferred using a tweezer with the side to be coated facing up in an empty 100 mm diameter PTFE dish, before filling it up with 20 mL of 1 wt% ascorbic acid solution. Similarly, the dish was placed on an orbital shaker at 50 rpm for 30 min. After this step, the white membrane turned slightly yellowish brown indicating the presence of silver nanoparticles. The membrane was then washed three times in 100 mL of DI water before drying the membranes in a convention oven, specifically the Binder FD series, to remove the moisture at a temperature of 70 °C for a duration of 1 h.

2.3. Fabrication of janus membrane on different surface structure

The commercial PES membrane was shiny on one side and dull on the other. Field-emission scanning electron microscope (FESEM) indicates clear distinctions in the different membrane surface structures as shown in Fig. 1. The PES and Ag-PES membranes were converted into Janus membranes via two steps, namely, a PDMS-coating process to convert the hydrophilic PES to a hydrophobic membrane, and a photothermal conversion of one surface to form laser-induced graphene (LIG) via laser irradiation. The sequence of the two steps was varied to optimize the membranes for MD.

The application of a PDMS coating was carried out via vacuum filtration of 5 mL of solution, which was made of 2 wt% Sylgard 184 PDMS in a 10:1 mix ratio by volume with the curing agent (Dow Corning) dissolved in (R)-(+)-Limonene (Sigma-Aldrich; a green solvent) [57]. The solution was left in contact with the membrane for a duration of 60 s before the vacuum pump was initiated. The modified (PDMS-PES) membrane was then subjected to a curing process in a convention oven (Binder FD) at a temperature of 120 °C for 12 h.

The LIG layer was formed by exposing the membrane surface to a 200 mW laser with a wavelength of 405 nm via a Totem S laser engraver (Two trees 3D), which moved across the membrane surface area of 90 mm long and 55 mm in width line-by-line at a speed of 25 mm/s. Fig. 2 (a and b) shows the typical photographs images of PES membranes before and after laser irradiation and Fig. 2 c shows the FESEM cross-section image of the LIG membranes, which represent the typical layer in the LIG membranes used in this study. The photothermal reaction formed a LIG layer on the membrane surface. Meanwhile Fig. 3 shows the schematic diagram for step-by-step preparation of LIG membranes for using shiny or dull sides of PES membranes surfaces. Table 1 presents an overview of the membranes utilized in this study, including details of their modifications.

2.4. Janus membrane characterization

2.4.1. Field emission scanning electron Microscopy (FESEM) imaging

To visualize the morphologies of the membranes, FESEM (JEOL JSM-6701 F) images were taken. This imaging technique provided detailed analysis of the membrane surface structure and allowed for visual comparison before and after the MD process. To ensure optimal imaging conditions and mitigate electron build-up during FESEM imaging, a thin layer of platinum (<10 nm) was applied to all the samples. This coating process involved the use of a sputter coater (JEOL JFC-1200) for a duration of 90 s at a current of 10 mA. Prior to FESEM imaging, platinum coating was applied to the samples. This process was conducted under high-vacuum conditions of 9.63×10^{-5} Pa and an accelerating voltage of 5 kV.

2.4.2. Thermogravimetric analysis (TGA)

To examine the thermal stability of the membranes, TGA (TA

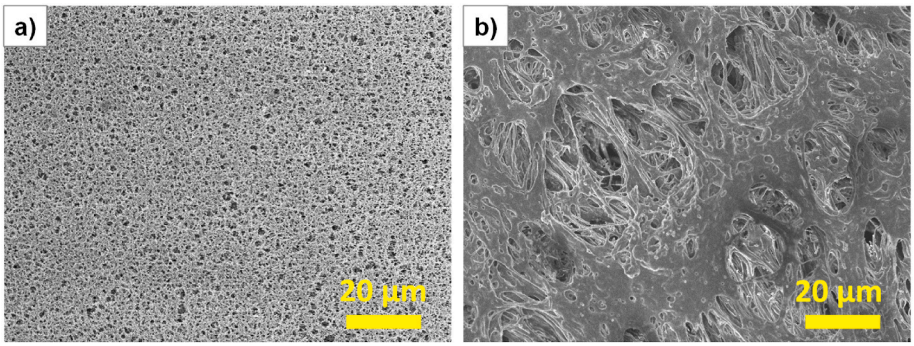

Fig. 1. FESEM images of the PES membrane surface: (a) shiny side and (b) dull side.

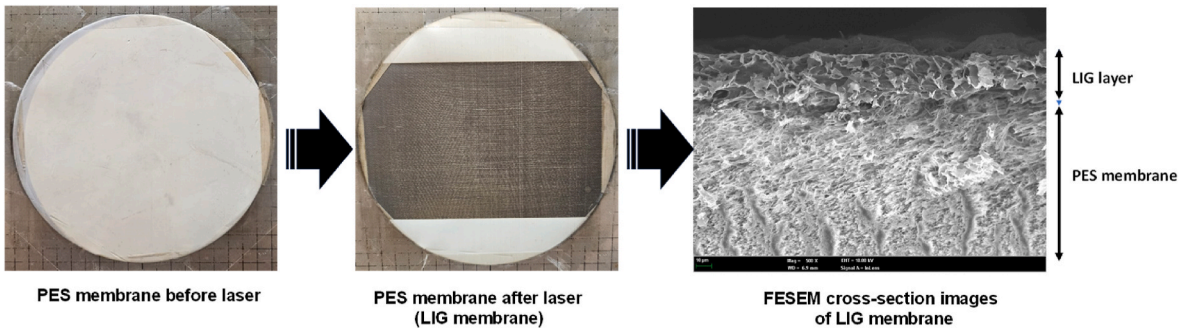

Fig. 2. (a and b) The typical photographs images of PES membranes before and after laser irradiation, and (c) shows the FESEM cross-section image of the LIG membranes.

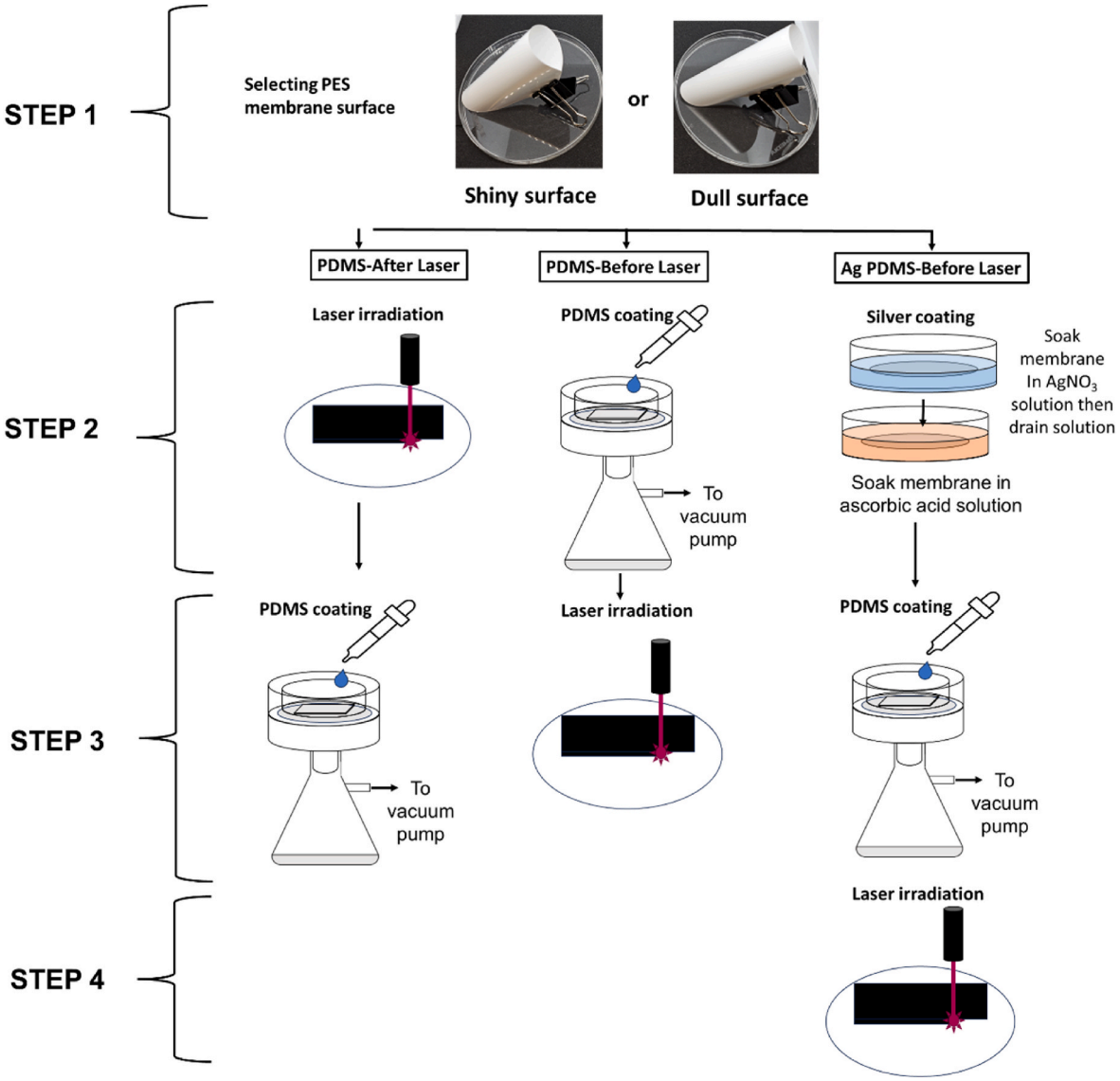

Fig. 3. Schematic diagram for step-by-step preparation of LIG membranes for using shiny or dull sides of PES membranes surfaces.

instruments SDT Q600) was utilized in this study. 5 mg of the membrane sample was placed into the crucible that was placed into the TGA, which was initially set to run isothermally at 100 °C for 5 min, after which the temperature was gradually ramped up at a rate of 10 °C min^{-1} until reaching a final temperature of 800 °C under N_2 purge gas at a flow rate of 100 mL/min.

2.4.3. *Raman spectroscopy*

To investigate the surface of the samples, a Raman Spectrometer (Renishaw in Via Reflex) was utilized. A 514 nm laser source operating at a power of 2.5 mW was directed onto the sample surface using a 20× objective to achieve the proper focus.

Table 1
Summary of membranes used in this experiment and their modifications.

Naming	Silver coated	Surface exposed to laser	PDMS coated
PDMS-BLSS	No	Shiny	Before laser exposure
PDMS-ALSS	No	Shiny	After laser exposure
PDMS-BLDS	No	Dull	Before laser exposure
PDMS-ALDS	No	Dull	After laser exposure
Ag PDMS-BLSS	Yes	Shiny	Before laser exposure
Ag PDMS-BLDS	Yes	Dull	Before laser exposure

2.4.4. X-ray photoelectron spectroscopy (XPS)

The signals from C 1s, O 1s, and S 2p and Si 2p and Ag 3 d were obtained using a Kratos Axis Supra XPS spectrometer (Kratos Analytical). The elements binding energy were fitted to the experimental data to analyze and identify the corresponding signals. The samples were thoroughly dried under vacuum at room temperature to ensure complete removal of any residual moisture, before being subjected to an ultra-high vacuum of 10^{-9} bar to conduct the measurements.

2.4.5. Capillary flow porometry (CFP)

The pore-size distribution (PSD) of the membranes was analyzed using a capillary flow porometer (CFP 1500 A, Porous Material. Inc.). The process involves mounting the sample into the sample holder before adding a few drops of Galwick™ wetting liquid. After that, the wetted sample placed on the sample holder was directed into the chamber of the porometer for analysis. Nitrogen gas was used as the inert gas to displace the wetting liquid through the pores of the membrane.

2.4.6. Surface temperature measurement

To analyze the impact of different heating techniques such as Joule and photothermal heating on the surface of the membrane, an infrared (IR) thermal imaging camera (Cat S60) equipped with Forward Looking InfraRed (FLIR) Lepton Infrared Radiation (IR) sensor was used to capture thermal images of the surface temperature of the LIG modified Janus membrane. To standardize the process, the thermal images were captured 30 s before and after heating using Joule or photothermal heating. Joule heating was performed by supplying AC power input of 15 W at 250 Hz. The photothermal heating was performed at a power density of 3 Sun or 3000 W/m^2.

2.5. Experimental study

The cross-flow MD experimental filtration setup was conducted to determine the impact of various factors affecting the performance of MD. Factors such as difference in the degree of laser etching, heating technique, applied input power for heating, and the rate of feed. The flux was monitored, as well as the specific heating energy and the single-pass heat utilization efficiency.

2.5.1. Experimental design and setup

In this study, bespoke tailor-made two-channel cross-flow membrane module made of acrylic was employed. Detailed specifications of the module are listed in Table S2. As illustrated in Fig. 4, the modified membranes (Table 1) were each carefully positioned within the membrane module before placing the titanium foil electrodes on opposite ends of the membrane perpendicular to the feed and distillate flow, with 6.5 cm between them. The active membrane area was 0.00334 m^2 (i.e., length 63 mm and width 53 mm). To support the membrane and to enhance the turbulence near the active membrane surface in both the inlet (feed) and outlet (distillate) channels, a polypropylene spacer (Sterlitech) was employed in the flow channels. The detailed specifications of the spacers are listed in Table S3. These spacers were reused consistently for the entirety of the study.

The experimental setup of the DCMD employed in this study is illustrated in Fig. 5. A peristaltic pump (Masterflex L/S Digital Drive)

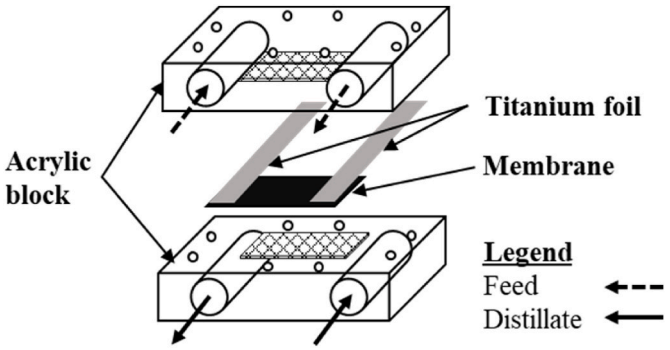

Fig. 4. Diagram illustrating the arrangement of the acrylic membrane module employed in this study.

was utilized to continuously circulate the feed and distillate streams counter-currently into the membrane cell. The feed tank was a stainless-steel tank of 2 L placed in a temperature-regulated recirculator (Julabo ME). The temperature was maintained at 25 °C. Masterflex Norprene tubing was used to circulate the feed between the membrane cell and the stainless-steel feed tank. The feed flow rate was maintained at 10 mL/min, giving a flow velocity in the feed channel of 4.7 cm/min. The feed either undergoes photothermal, electrothermal or both types of heating. In the photothermal heating experiments, the feed was subjected to heating as it flowed past the membrane. This heating was achieved using a solar lamp with a power equivalent to one-sun, generated by a xenon light source (Ceaulight CEL-HXF300-T3).

The electrothermal heating of the LIG membranes was achieved by applying an AC current through a pair of titanium electrodes connected to the electrically conductive surface of the membrane. This AC current generated joule heating within the membrane, causing the temperature to increase. The choice of using an AC current for electrothermal heating was motivated by the need to avoid rapid electrochemical degradation of the graphene on the LIG Janus membrane in an ionizable medium, because the high-voltage direct current (DC) required for generating the necessary power for heating can lead to accelerated degradation of the graphene [58]. AC power (Ivytech APS-4000 B) was supplied at 250 Hz directly to the titanium foil electrodes. The input power supplied for electrothermal heating was calculated by multiplying the input voltage and the current.

A recirculating chiller (Julabo ME) was utilized to maintain the distillate at a lower temperature. The distillate was then recirculated between the membrane cell and distillate tank using Masterflex Tygon *E*-LFL tubing. The recirculation was set at a flowrate of 200 mL/min, causing the flow in the distillate channel of membrane cell to be 94 cm/min.

The cylindrical acrylic distillate tank had a volume of 1 L and overflowed into another tank that sat atop a mass balance (Mettler-Toledo ME4002) to quantify the distillate flux. To ensure a consistent sodium chloride (NaCl; Merck-Millipore CAS No.7647-14-5) concentration of 35 g/L, a peristaltic pump (Masterflex L/S Digital Drive) was used to periodically recycle the distillate collected in the overflow tank every 1 h for a duration of 1 min. An in-line conductivity meter (Mettler Toledo Cond Sensor 3/4NPT 0.1C Mnl 2 ISM) was inserted into the distillate tank, allowing real-time monitoring of any leak.

2.5.2. MD operating procedures

The MD experimental protocol is described as follows. Firstly, the prepared modified membrane was carefully placed in the membrane cell together with titanium foil electrodes positioned 6.5 cm apart on the active side of the membrane. Next, the feed containing 35 g/L of NaCl was circulated at a flow rate of 10 mL/min, giving a flow velocity in the feed channel of the membrane cell of 4.7 cm/min. Simultaneously, a flow rate of 200 mL/min of DI water was circulated within the distillate

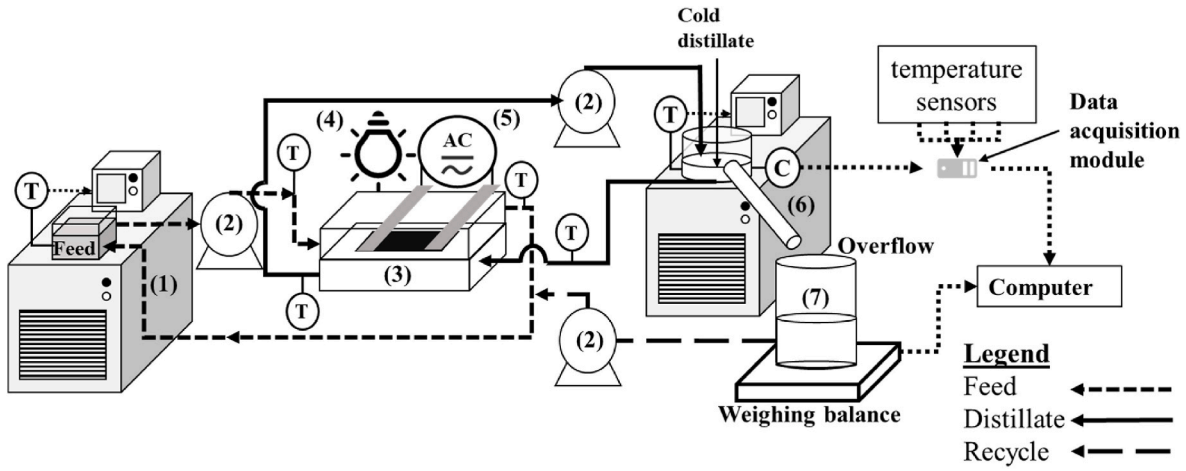

Fig. 5. Schematic representation of the experimental setup employed in this study, including components such as (1) a 2 L rectangular stainless steel tank containing the NaCl feed cooled by a recirculating chiller, (2) three peristaltic pumps; for feed and distillate recirculating loop, and recycling line, (3) a custom-made acrylic membrane module, (4) solar simulator atop the membrane module, (5) an AC power supply connected to the titanium electrodes for electrothermal heating of the membrane, (6) a 1 L acrylic cylinder with a spout containing the distillate kept cool using a recirculating chiller, and (7) a beaker containing the distillate overflow placed on a weighing balance. T and C represent the temperature and conductivity sensors.

loop, resulting in a flow velocity in the distillate channel of 94 cm/min.

Throughout the experimental runs, the feed and distillate tanks temperatures were kept constant at 25 °C and 20 °C, respectively. The power of the solar simulator was calibrated and adjusted to provide a power density of 3 suns, which is equivalent to 3000 W/m^2, using a radiance meter (Melles Griot, 13PEM001). The higher power was utilized to account for the small surface area of the laboratory setup in order to generate a measurable distillate flux every 5 min. Electrothermal heat was applied directly to the active area of the LIG-modified Janus membrane using an AC power of 15 W; higher power would risk breaking down the LIG surface. Finally, data logging software (National Instruments) was used to capture the parameters of interest, such as temperatures at the inlets and outlets of the membrane cell, mass of the distillate accumulated, and conductivity of the distillate. These measurements were taken every 5 min throughout the entire 3 h run of each experiment. The conductivity of the distillate is measured to be less than 10 μS at the start of every experiment when the conductivity stabilizes, and it did not exceed 15 μS throughout the experiment. The feed conductivity was measured to be about 32,200 μS at the start of the experiment. This translates to a salt rejection of 99.95–99.97 %.

2.5.3. Flux and energy calculations

The flux trend with time, specific heating energy, and single-pass heat utilization efficiency were used to assess the overall performance of the MD process. Flux, J (L/m^{2}h), was calculated using Eq. (1):

$$J = \frac{\Delta M_{Overflow}}{\rho_d \times \Delta t \times A_m} \quad (1)$$

where $\Delta M_{overflow}$ (kg) is the mass of distillate accumulated over a time period of Δt (h), ρ_d (kg/L) is distillate density and A_m (m^2) is the active membrane area.

The specific heating energy, Q_{sh} (kWh /L), measures the amount of heat energy required per unit volume of distillate produced. It reflects energy efficiency and was calculated using Eq. (2):

$$Q_{sh} = \frac{Q_{in}}{J} \quad (2)$$

where Q_{in} (kW/m^2) is the power input, which was calculated using Eq. (3):

$$Q_{in} = \frac{V \times I}{A_m} \quad (3)$$

where V (V) is the applied voltage, and I (A) is the current.

The single-pass reactor heat utilization efficiency (HUE_{sp}) represents the percentage of input energy that is effectively utilized for vapor production and was calculated using the following Eq. (4) and Eq. (5):

$$HUE_{sp} = \frac{Q_v}{3.6(Q_{in} \times A_m)} \times 100\% \quad (4)$$

where Q_v represents the rate of heat energy required to generate flux:

$$Q_v = J \times \rho_d^{-1} \times A_m \times \Delta H_v \quad (5)$$

where ΔH_v is the specific heat needed for vaporization (i.e., 2453 kJ/L at 20 °C).

3. Results and discussion

3.1. Effect of membrane structure and coating sequence on MD performance

Fig. 6 illustrates the variation in MD performance resulting from the converting of different surfaces of the PES membrane to LIG operated under different heating methods: (a) flux, (b) single pass heat utilization efficiency, HUE_{sp}; and (c) specific heating energy, Q_{SH}. The shiny surface membranes (PDMS-BLSS) showed an overall higher flux and HUE_{sp}, and a lower Q_{SH} compared to the dull surface membranes (PDMS-BLDS). These results are also consistent with PDMS membranes after modification with silver. On the other hand, the effect of coating sequence was inconclusive. Specifically, for the sequence of PDMS coating applied after the LIG formation, MD performance worsened for the shiny surface of the membrane (PDMS-ALSS), whereas MD performance improved for the dull surface of the membrane (PDMS-ALDS) as clearly shown in Fig. 6a.

Since membrane pore size is one of the key membrane parameters that affect flux, liquid displacement porometry (LDP) was used to characterize the pore size distributions of all the membranes. FESEM surface and cross-section images in Fig. 7 demonstrate both shiny and dull sides of membrane-coated PDMS before and after LIG formation confirming that the lasing led to the formation of larger pores and irreversible changes in the nanoscale features. The formations of bigger pores after LIG formation are clearly shown by FESEM images in Fig. 7 (d, e, h and i). On top of that, based on pore-size distribution (PSD) analysis shown in Fig. 8a, the LIG formed on the PDMS coated-shiny

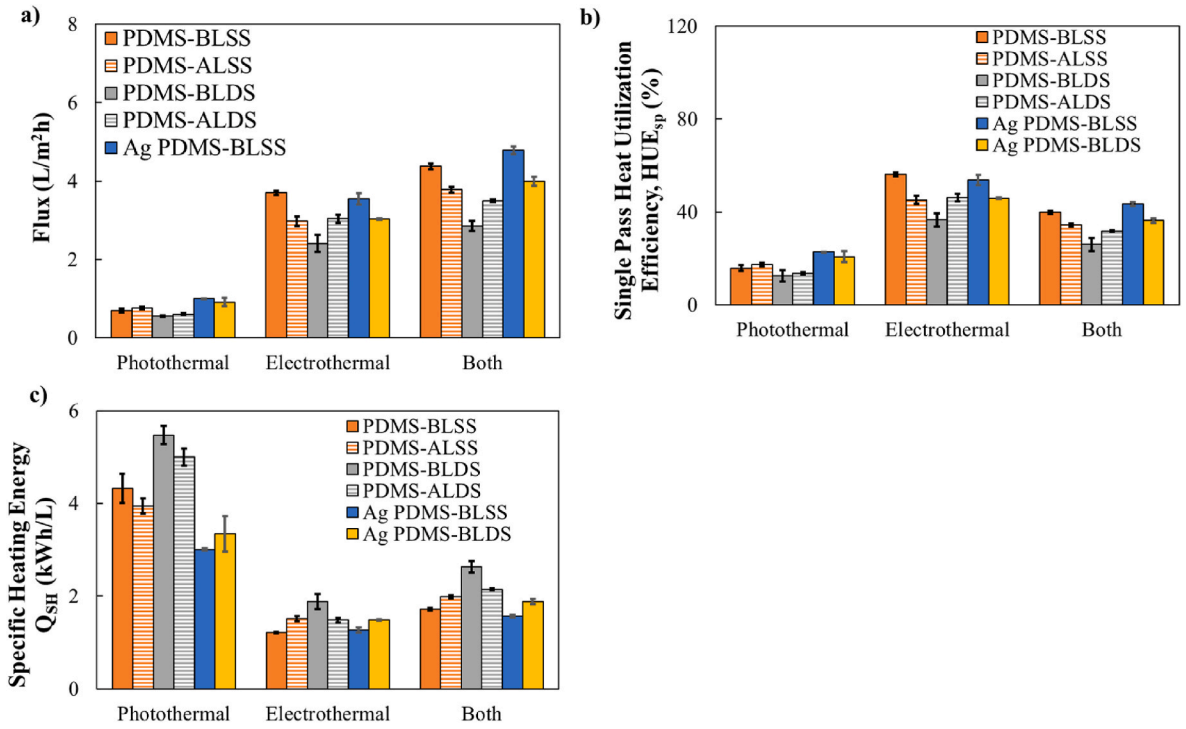

Fig. 6. Experimental results of the modified membranes used in the DCMD setup operated under different heating methods: (a) flux (L/m^{2}h), (b) single pass heat utilization efficiency, HUE_{sp} (%), and (c) specific heating energy, Q_{SH} (kWh/L).

membrane surface after LIG formation (PDMS-ALSS) exhibited larger pores (0.22–0.62 μm) as compared to PDMS coated membrane before LIG formation (PDMS-BLSS) (0.16–0.47 μm). However, the differential permeability (%) for these membranes is relatively lower than dull side-membrane surfaces indicating a wider range of pore sizes formed. This observation prompted further analysis of the wettability of the membranes through contact angle measurements. Interestingly, although PDMS-ALSS had the largest nominal pore size and reduced contact angle, it did not obtain the highest flux as illustrated in Fig. 6a.

As shown in Fig. 8b, upon PDMS coating after LIG formation, the contact angle for shiny membrane surface slightly reduced (PDMS-ALSS) from 138.1° to 129.9°, which is opposite to contact angle of dull membrane surface (PDMS-ALDS) (from 124.1° to 134.1°). The decrease in contact angle for PDMS-ALSS has increased the hydrophilicity properties and thus plausibly caused the relative lower flux of the membrane. In contrast, the doping of silver on the PDMS membrane surface before LIG exposure reduced the contact angle of the dull side membrane (Ag PDMS-BLDS) from 142.6° to 134.2°. Silver nanoparticles have been reported widely have increased the hydrophilicity of polymeric membranes due to their nanostructure which positively affects the membrane flux [59,60]. However, in the contact of MD applications, the hydrophilic property of the membrane is unfavourable as the membrane properties should own a hydrophobic property to obtain and maintain higher flux.

The trend in membrane hydrophobicity is well-correlated with MD performance, with higher hydrophobicity, the membrane could give better performance. Based on the flux equation, J, can be quantified by the following Eq. (6) [13,61]:

$$J = C_m \frac{dP}{dT}\left(T_{f,m} - T_{d,m}\right) \tag{6}$$

where C_m is the mass transfer coefficient, and $T_{f,m}$ and $T_{d,m}$ are the temperatures of the feed-side and distillate-side of the membrane.

The effect of the vapor pressure driving force can be isolated by assuming that the vapor pressure driving force resulting from the temperature difference between the membrane surface on the feed side and the membrane surface on the distillate side is same for all membranes. The theoretical flux, J_{Theo}, can be determined by multiplying a reference flux by the ratio of the mass transfer coefficient of the membrane of interest normalized by that of the reference membrane as shown in Eq. (7).

$$J_{Theo} = J_{Ref} \times \frac{C_m}{C_{m,Ref}} \tag{7}$$

Calculating the Knudsen number, K_n, and mean free path, λ, using Eqs. (8) and (9) [13,62–64], respectively, allows for determining the flow regime in the pore:

$$K_n = \frac{\lambda_w}{D_{pore}} \tag{8}$$

$$\lambda_w = \frac{k_B T}{\sqrt{2}\pi \bar{P} {\sigma_w}^2} \tag{9}$$

where K_B is Boltzmann constant, T is membrane temperature, $\bar{P}$ is average pressure within the membrane pore, and σ_w is the hard-shell diameter of a water molecule. it was determined that the vapor flow within the membrane pore, D_{pore}, falls within the transition region ($0.01 < K_n < 1$ or $\lambda < D_{pore} < 100\lambda$). In this region, water vapor molecules both collide with each other and diffuse through the air film. Therefore, the mass transfer in this system takes places through an amalgamation of the Knudsen diffusion and ordinary diffusion mechanism. The mass transfer coefficient across the membrane, C_m, can be verified by the following Eq. (10) and Eq. (11).

$$C_m = \frac{\pi}{RT}\frac{1}{\tau\delta}\left[\left(\frac{2}{3}\left(\frac{8RT}{\pi M_w}\right)^{\frac{1}{2}} {r_{pore}}^3\right)^{-1} + \left(\frac{PD}{P_a} {r_{pore}}^2\right)^{-1}\right]^{-1} \tag{10}$$

$$PD = 1.895 \times 10^{-5} T^{2.072} \tag{11}$$

where P is the total pressure and D is the diffusion coefficient of water vapor in air.

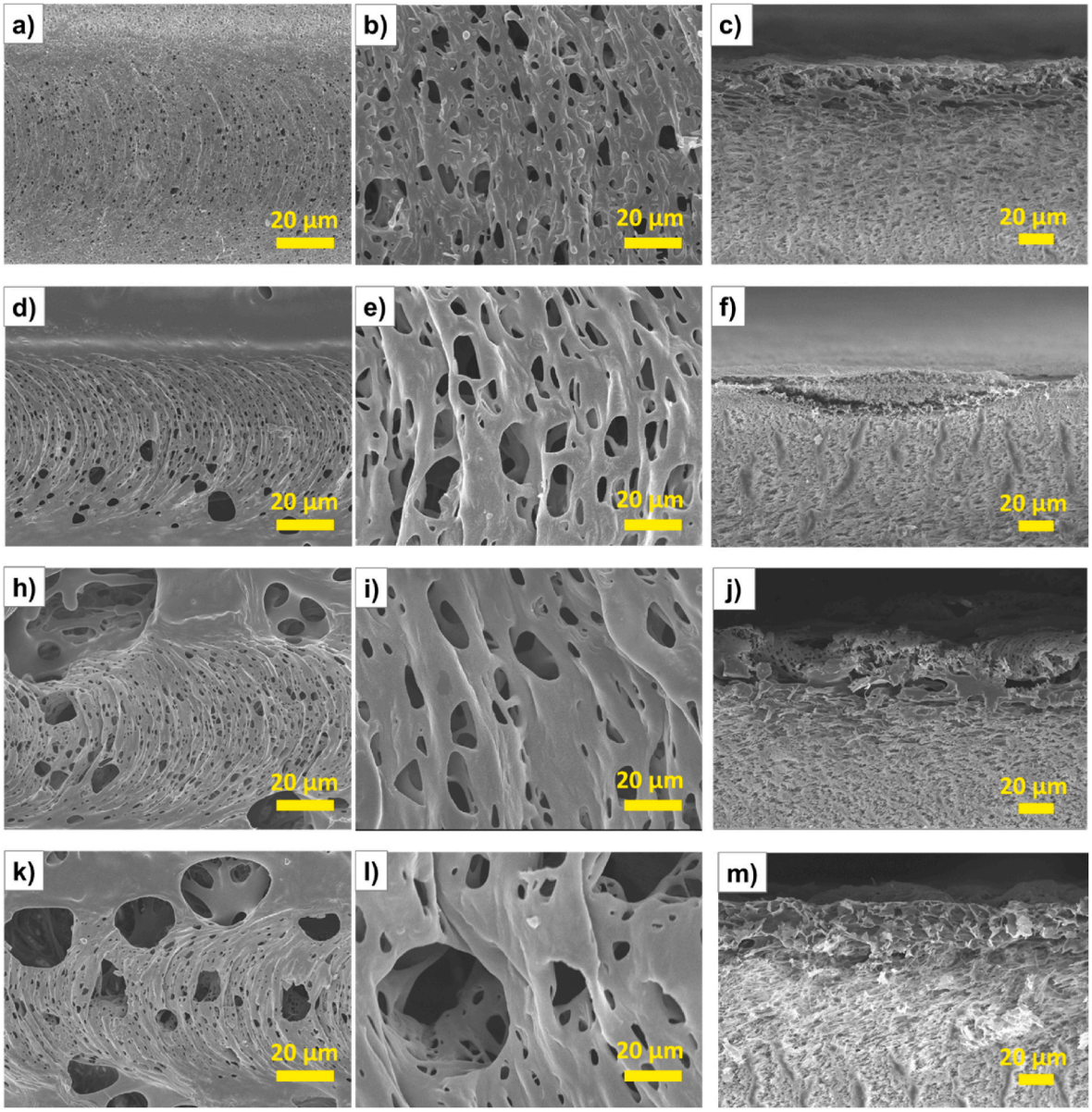

Fig. 7. FESEM surface images of PDMS-BLSS (a, b), PDMS-ALSS (d, e), PDMS-BLDS (h, i), PDMS-ALDS (k, l), and FESEM cross-section images of PDMS-BLSS (c), PDMS-ALSS (f), PDMS-BLDS (j), PDMS-ALDS (m).

Further analysis was carried out using the theoretical flux prediction equations (Eqns. (6)–(11)) [13,61]. Considering the measured contact angle and pores size, and assuming the temperature difference across the membrane remains the same, the discrepancy between the theoretical and experimental fluxes were in the range of 8.3–55.3 % (Fig. 9a–c). The theoretical fluxes are smaller than experimental ones in all cases except for PDMS-ALSS, which can be attributed to the lower surface porosity of PDMS-ALSS (Fig. 9b). Despite PDMS-ALSS having larger pore sizes, the 35.7 % lower porosity (estimated using FESEM image analysis) reduced the flux significantly. Correcting for this lower porosity, the theoretical fluxes of PDMS-ALSS when operating in different heating modes are 16.8–31.4 % lower than that obtained experimentally as shown in Figs. 6 and 9.

This indicates the PDMS coating sequence results in a drastic change in membrane performance, particularly when applied to the shiny side membrane surface compared to the dull side membrane surface. With respect to the shiny side of the membrane surface, applying a PDMS coating before the formation of the LIG process (PDMS-BLSS) led to a reduction in flux by 0.3–25.5 % (Fig. 6a), an increase in specific heating energy (Q_{SH}) by 0.3–33.8 % (Fig. 6b), and a reduction in single-pass reactor heat utilization energy (HUE_{sp}) by 0.3–25.5 % (Fig. 6c) as compared to coating of PDMS after the formation of LIG (PDMS-ALSS). On the other hand, the dull side membrane surface had more dispersed big pores which are less susceptible to pore-blocking during PDMS coating as shown in Fig. 7e and g.

Since the effect of the vapor pressure driving force is isolated in the calculations contributing to these results, the discrepancy between theoretical and experimental flux could be attributed to the difference in heating performance of the membranes resulting in a difference in vapor pressure driving forces across the membrane. For the PDMS LIG membranes that were not doped with Ag, the discrepancy between the theoretical and experimental flux was less significant in the photothermal experiments compared to that for electrothermal heating (Fig. S1). This indicates that the structure of the membranes had a smaller effect on the heating mode (i.e., photothermal versus electrothermal). In addition, infrared thermal images taken before and after 30 s of light irradiation show an average surface temperature difference among the PDMS LIG membranes ranged from 26.9 to 32.4°C (Fig. 10),

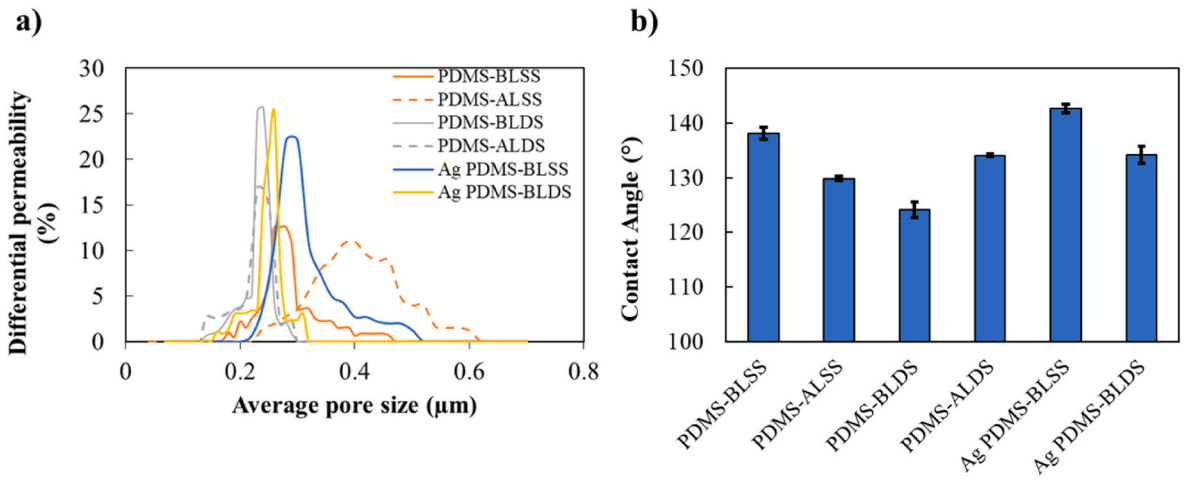

Fig. 8. (a) The pore size distribution (PSD) analysis and (b) the contact angle measurement for all the prepared membranes.

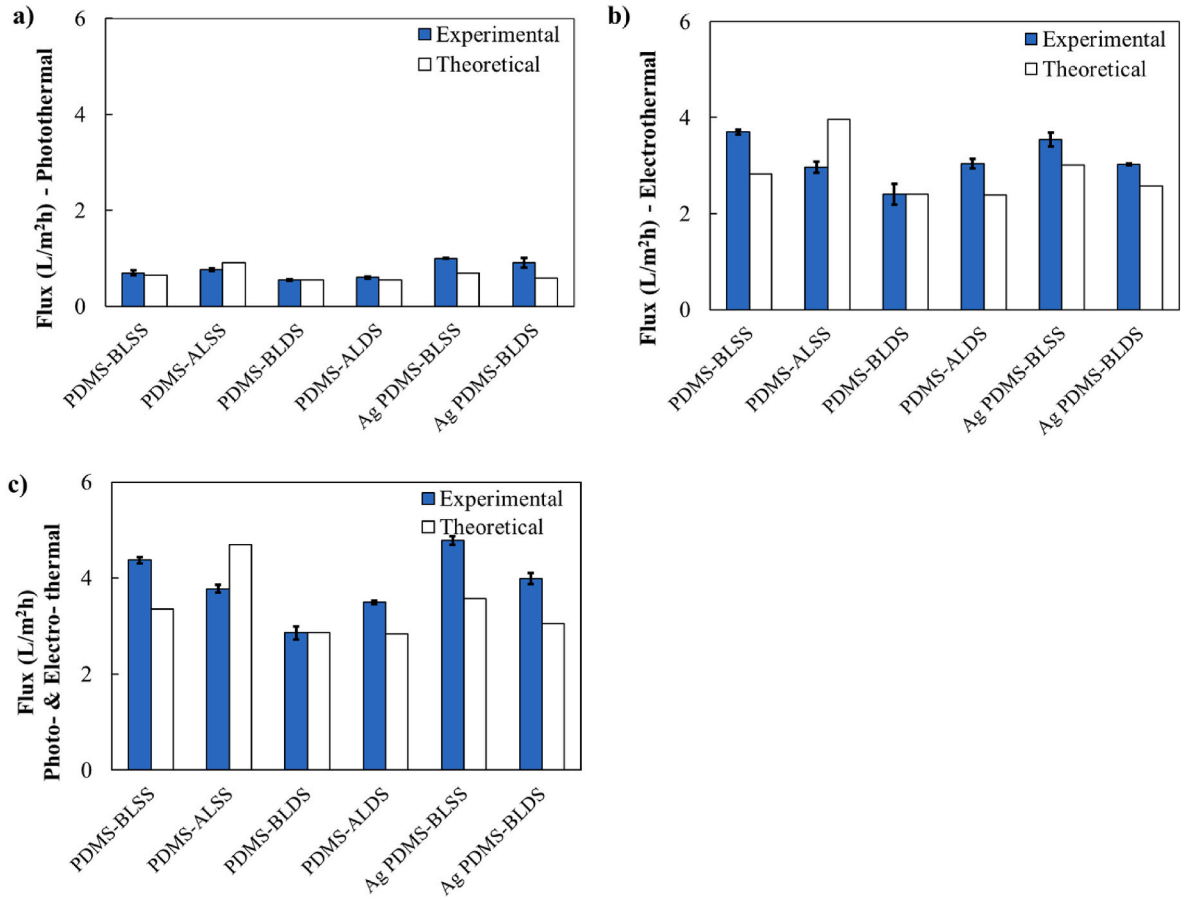

Fig. 9. The comparison of the experimental and theoretical flux of the membranes operating in (a) photothermal heating, (b) electrothermal heating and (c) simultaneous photo- and electro-thermal heating modes.

while that taken before and after 30 s of passing 15 W of electricity show a higher average surface temperature difference among the PDMS LIG membranes of 52.2–67.4 °C (Fig. 11). Therefore, the LIG on the shiny side of the membrane (PDMS-ALSS) gave an overall higher photo- and electro-thermal heating performance compared to that on the dull side of the membrane (PDMS-ALDS).

The improved electrothermal heating property of the membranes can be attributed to the LIG formed on the membranes. Raman spectroscopy was employed to assess the presence and quality of graphene following the laser etching process. The Raman spectra of LIG (Fig. 12a) indicate the presence of characteristic peaks associated with graphene in the membranes that were coated with PDMS before and after being exposed to the laser. These peaks were observed at approximately 1330 cm^{-1} (D peak), 1578 cm^{-1} (G peak), and 2600 cm^{-1} (2D peak). More specifically, the D peak in the Raman spectra is attributed to defects in the sp2 carbon bonds of graphene, the G peak corresponds to the in-plane vibrations of sp2-bonded carbon atoms in the graphene structure, and the 2D peak arises from a two-phonon lattice vibration in graphene. These

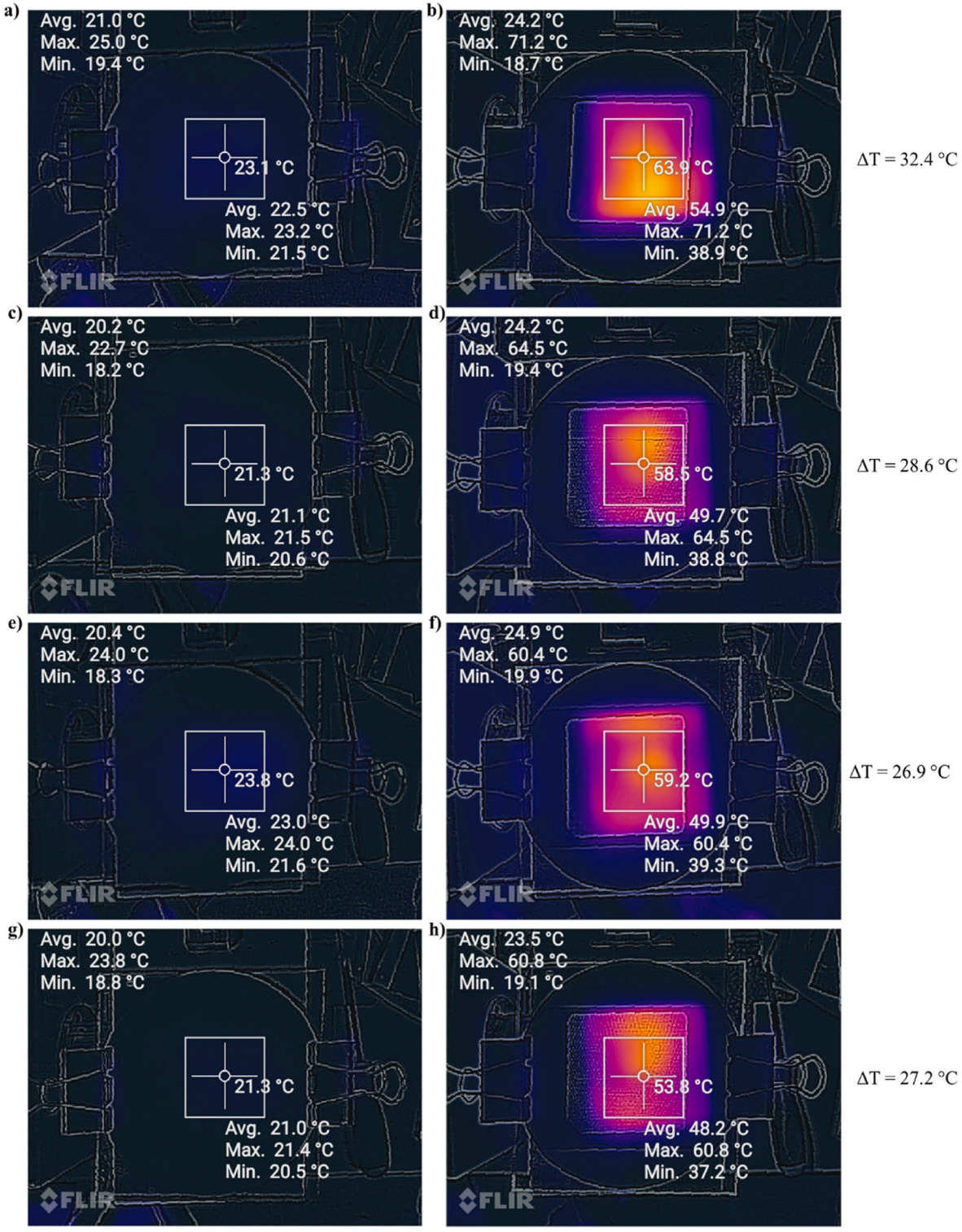

Fig. 10. IR thermal images of membrane surface of PDMS-BLSS (a, b), PDMS-ALSS (c, d), PDMS-BLDS (e, f), PDMS-ALDS (g, h); left column: before light irradiation, and right column: after 30 s of photothermal/light irradiation from solar simulator.

characteristic peaks provide evidence for the presence of graphene in the membranes coated with PDMS before laser etching [65,66]. However, these peaks were not observed in the membranes which were coated with PDMS after exposing to the laser (PDMS-ALDS and PDMS-ALSS). The ratios of peak intensities, such as I_D/I_G and I_{2D}/I_G, as well as the full width at half maximum (FWHM) of the 2D peak in the Raman spectrum of the sample can be used to determine the quality of the graphene. A lower I_D/I_G ratio and a higher I_{2D}/I_G accompanied with a high FWHM of ~70 cm^{-1} gives a higher-quality graphene [66]. The PDMS-BLSS had a I_D/I_G ratio of 0.4, I_{2D}/I_G ratio of 0.6 and an FWHM of 74 cm^{-1}, while the PDMS-BLDS had a I_D/I_G ratio of 0.71, I_{2D}/I_G ratio of 0.64 and an FWHM of 66 cm^{-1}. The close-up of the Raman spectra of PDMS-BLSS and PDMS-BLDS as shown in Fig. 12b, the former having more prominent characteristic peaks associated with graphene, indicating higher graphene quality when LIG was formed on the shiny surface (PDMS-BLSS).

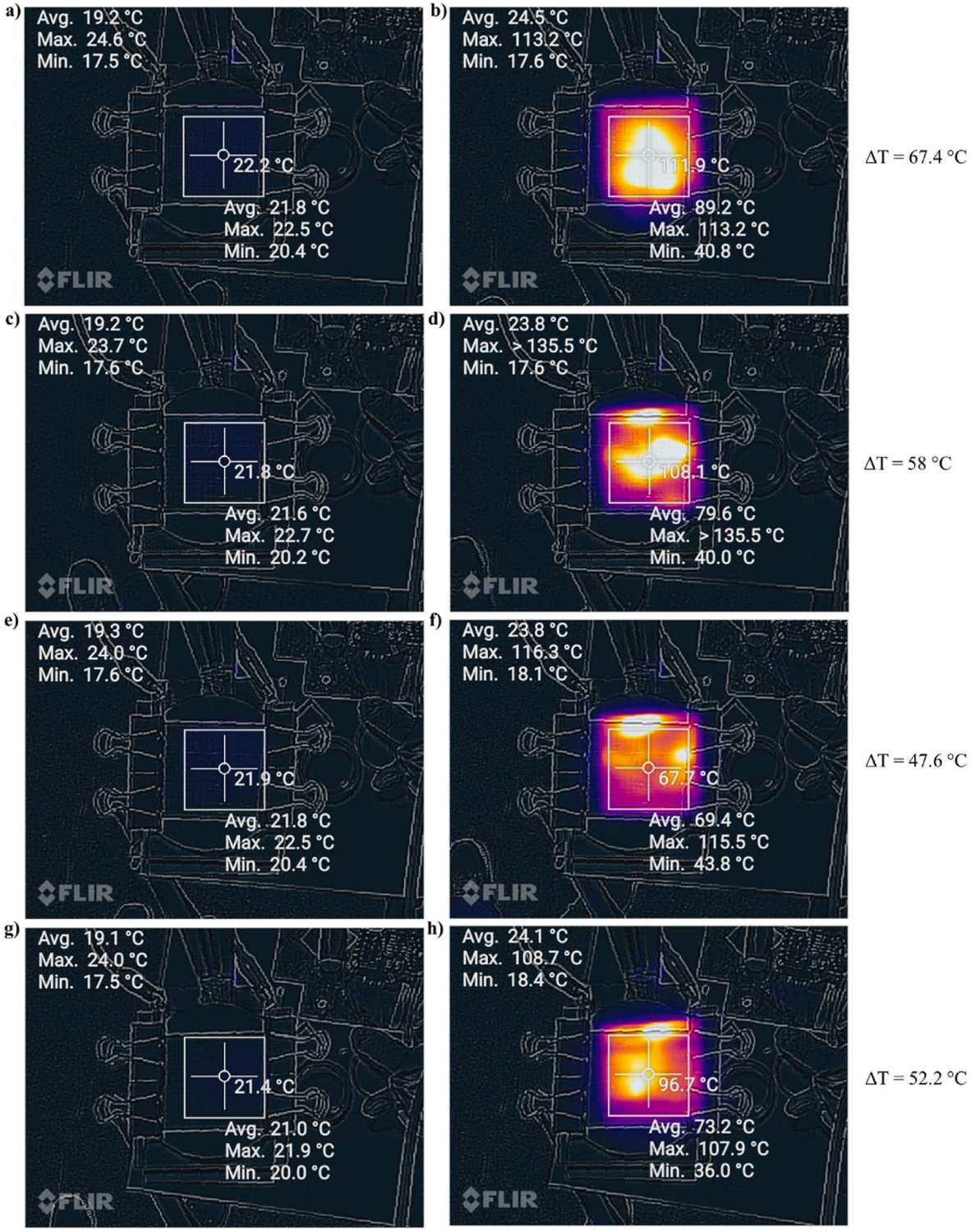

Fig. 11. IR thermal images of membrane surface of PDMS-BLSS (a, b), PDMS-ALSS (c, d), PDMS-BLDS (e, f), PDMS-ALDS (g, h); left column: before electrothermal heating, and right column: after 30 s electrothermal heating using the AC power source.

Further surface analysis using XPS (Table 2) shows that, despite the total carbon content being similar, a higher ratio of the area of the C1s peak at 284.8 eV to that of the C1s peak at 286.9 eV was observed for membranes with the shiny side converted to LIG (PDMS-ALSS and PDMS-ALDS), indicating more C–C bonds. The increased surface concentration of graphene, along with the improved quality of graphene observed in the Raman spectroscopy results, played a significant role in enhancing the electrothermal properties of the LIG membrane formed on the shiny side of the membrane.

3.2. *Effect of the addition of silver nanoparticles*

The silver loading was quantified using TGA, XPS and EDS (Table 3). The silver loading for the surface and within the membrane cross-section of the silver-doped LIG membranes on the shiny side (Ag PDMS-BLSS) was slightly higher than that on the dull side (Ag PDMS-BLDS)

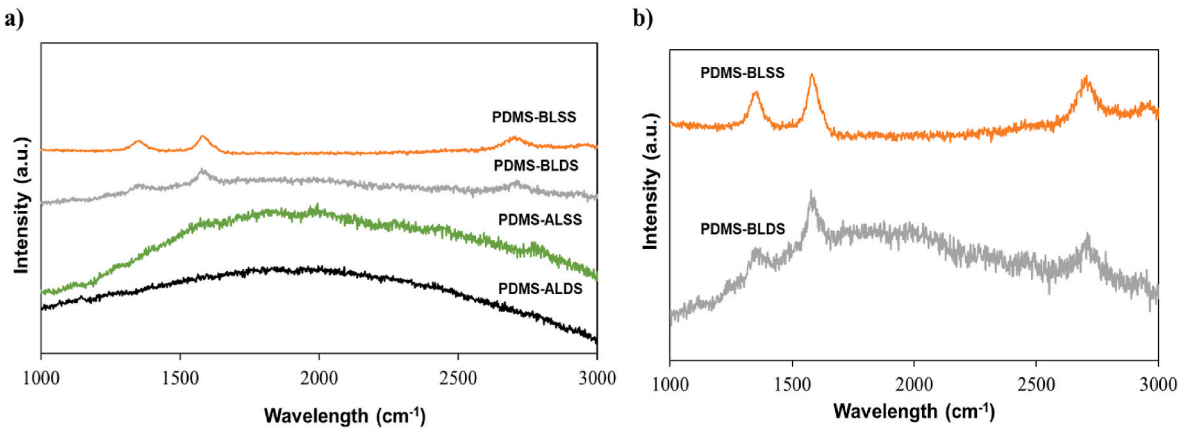

Fig. 12. Raman spectra of the: (a) undoped LIG Janus membranes and (b) close-up of the Raman spectra of PDMS-BLSS and PDMS-BLDS.

Table 2
Summary of surface mass concentration of the undoped LIG Janus membranes obtained through the XPS analysis.

Surface mass concentration (%)					
	Si 2p	S 2p	O 1s	C 1s	ratio
PDMS-BLSS	29.98	3.19	25.01	41.82	3.39
PDMS-ALSS	28.86	2.42	22.99	45.73	5.02
PDMS-BLDS	27.38	1.81	24.84	45.98	3.06
PDMS-ALDS	28.90	2.61	22.38	46.10	3.05

Table 3
Summary of silver mass concentration measured in the silver-doped membrane using XPS, EDS and TGA.

Mass concentration (%)				
	XPS	EDS (Surface)	EDS (Cross-section)	TGA
Ag PDMS-BLSS	9.81	4.30	4.00	6.84
Ag PDMS-BLDS	5.32	2.36	1.40	3.54

(Table 3). Further analysis of the EDS mapping of the cross-section of both silver-doped LIG membranes shows that silver is gathered on the active surface of the membrane for Ag PDMS-BLSS membrane (Fig. 13b), while silver is evenly distributed within the thickness of the membrane for Ag PDMS-BLDS membrane (Fig. 13e). Similarly, the silicon element was observed deeper in the membrane matrix for Ag PDMS-BLDS membrane (Fig. 13f) compared to Ag PDMS-BLSS membrane (Fig. 13c). This is attributed to the ease of flow of the $AgNO_3$ (silver nitrate) and ascorbic acid reagents into the larger pores of the dull surface of the membrane, allowing the silver nanoparticles to form evenly within the membrane matrix. However, this also allows the reagent and smaller particles to diffuse out of the membrane, thus reducing the silver loading. On the other hand, the smaller pores of the shiny surface of the membrane result in a slower flow of the $AgNO_3$ and ascorbic acid reagents, allowing silver nanoparticles to form and be trapped near the surface of the membrane.

Operating in the photothermal heating mode, the silver nanoparticles doped membranes gave a 43.1–65.8 % increase in flux compared to its counterpart without silver nanoparticles. The increase in flux was contributed by the enhanced photothermal heating properties

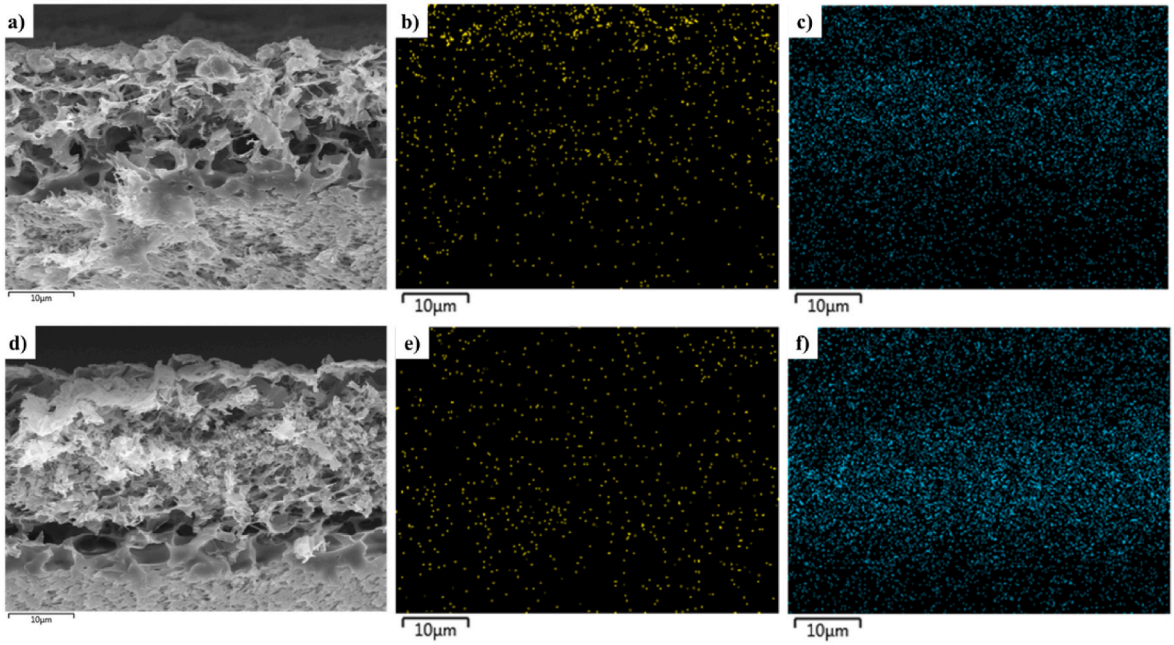

Fig. 13. The FESEM cross-section images of Ag PDMS-BLSS (a) and Ag PDMS-BLDS (d), and EDS mapping of Ag-Lα1 and Si K α1 for Ag PDMS-BLSS (b and c) and Ag PDMS-BLDS (e and f).

resulting from the surface plasmon resonance of the silver nanoparticles, which gave a higher average surface temperature difference of 41.4–46.5 °C before and after 30 s of light irradiation (Fig. 14) compared to the temperature difference of 26.9–32.4 °C observed for the LIG membranes without the silver nanoparticles (Fig. 10a, b, e, f). The superior photothermal heating and MD flux performance of the Ag PDMS-BLSS membrane compared to the Ag PDMS-BLDS membrane is attributed to the higher silver loading and high concentration of silver nanoparticles on the shiny surface where they can be exposed to more light.

One the other hand, as shown in Fig. 15, when 15 W of electricity was passed through the silver nanoparticles-doped membranes, the average surface temperature difference for before and after 30 s increased, ranging from 55.5 to 59.0°C, which is within the 47.6–67.4°C (Fig. 11a, b, e, f) observed in the LIG membranes without the silver nanoparticles. This indicates the presence of silver nanoparticles did not affect the electrothermal heating performance, as also shown in Fig. 6.

As shown in Fig. 16 operating MD in the concurrent photo- and electro-thermal heating modes using the silver-doped LIG membranes indicates a synergistic effect whereby the flux was higher than the addition of their fluxes obtained when operating with either heating mode (Fig. 6). This phenomenon can be attributed to the exponential relationship between the vapor pressure at the feed side and temperature, as described by Antoine's equation [67]. As the temperature increases, the vapor pressure increases exponentially, leading to a non-linear increase in the flux. However, the HUE_{SP} and Q_{SH} of the concurrent heating system decreased and increased, respectively (Fig. 6), indicating that the higher flux was produced with a lower thermal efficiency. This is due to the low photothermal conversion efficiency within the membrane distillation cell as water absorbed, scattered and reflected the light, which affected how much of the incident solar light actually hit the membrane surface. Hence, where solar energy is readily available, it can be used in tandem with other surface heating techniques to produce higher flux compared to standalone solar membrane distillation.

3.3. Feasibility of simultaneous photo- and electro-thermal MD with LIG janus membranes

The green label of MD as a separation technology inevitably also relies on the efficiency of energy utilization. Traditional MD systems typically employ volumetric heating methods, which involve heating the entire feed, which represents a significant heat loss because the driving force for distillation depends only on the heat at the feed-membrane interface. Therefore, the ability to generate heat efficiently and effectively directly on the surface of the active membrane surface in MD systems offers the potential to bridge the water-energy nexus, by improving thermal efficiencies and temperature polarization which commonly plagues the MD system.

This surface heat can be generated via two main methods, namely, electrothermal and photothermal methods. However, solar heating alone is insufficient to cater for solar distillation due to the limit of the power density of the Sun at 1000 W/m^2, while electrothermal heating is limited to the current the conductive material can withstand before it degrades. By doping silver nanoparticles into LIG using the method described in this study allows the concurrent use of two independent heating methods onto a membrane surface, thus overcoming the limit of operating in either one of the heating methods. Furthermore, the surface temperature can be heated via simultaneous photo- and electro-thermal heating to a higher temperature without compromising the structural integrity of the membrane. As the temperature difference across the membrane increases, the overall flux in the MD system increases exponentially, and thus the synergistic coupling of simultaneous photo- and electro-thermal in MD makes solar-assisted MD more feasible for large-scale desalination by maximizing heat utilization while lowering heat loss to the bulk feed solution. This enhances the sustainability of MD for water purification.

This study focused on the optimization of photothermal conversion efficiency via embedding silver nanoparticles in LIG membranes via a dip-coating method, enhancing the electrothermal heating properties of these membranes, which builds on the previous study on using LIG

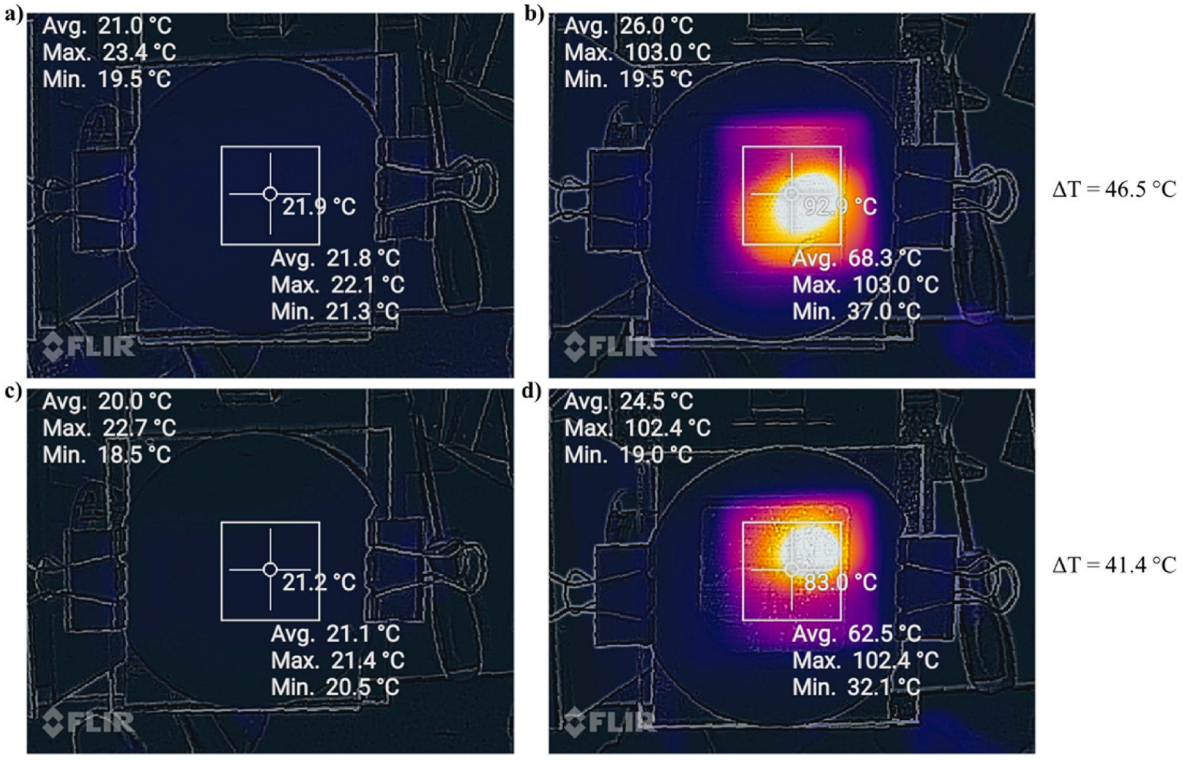

Fig. 14. IR thermal images of membrane surface of Ag PDMS-BLSS (a, b) and Ag PDMS-BLDS (c, d); left column: before light irradiation, and right column: after 30 s of photothermal/light irradiation from a solar simulator.

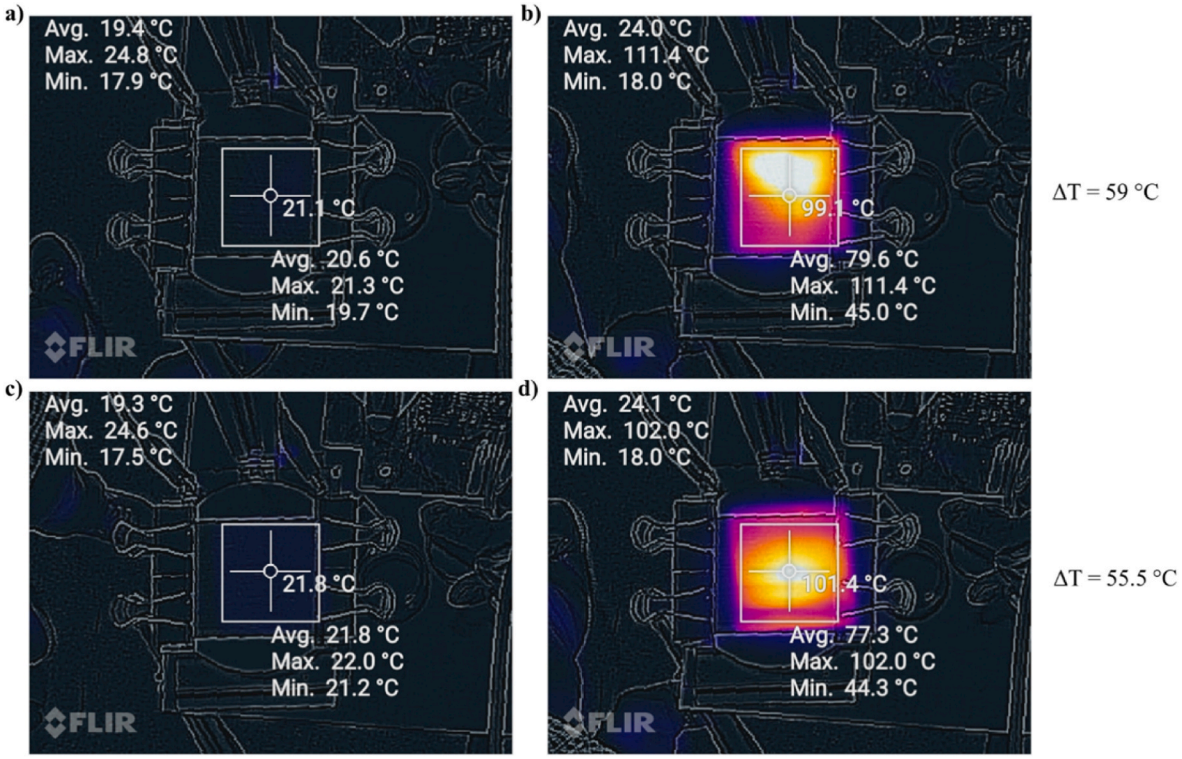

Fig. 15. IR thermal images of membrane surface of Ag PDMS-BLSS (a, b) and Ag PDMS-BLDS (c, d); left column: before of electrothermal heating, and right column: after 30 s of electrothermal heating using the AC power source.

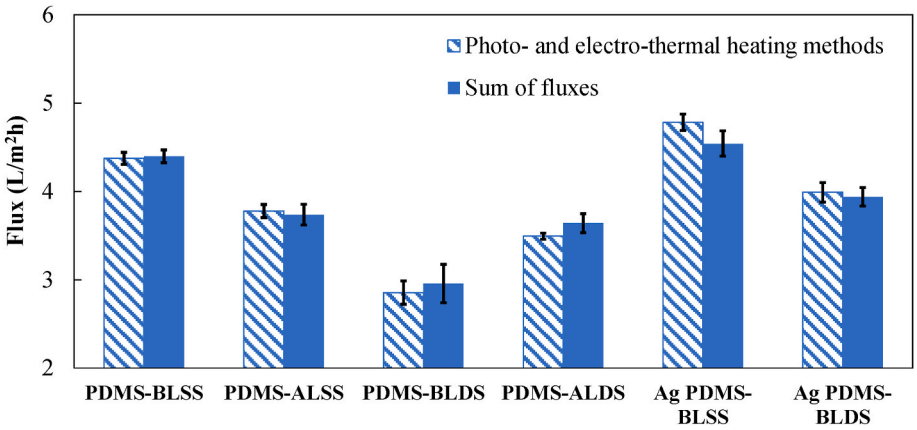

Fig. 16. The comparison of the simultaneous photo- and electro-thermal heating and sum of fluxes from individual heating methods.

membranes for electrothermal MD [68]. Furthermore, the addition of dip coating steps and laser irradiation steps to a roll-to-roll process of flat sheet membrane fabrication is highly feasible. This paves the way for embedding different materials in LIG membranes for different functions, such as improved catalytic activities, different surface wettability, selective affinity to different molecules for sensing applications, and photo responses for optical and optoelectronic applications.

Further studies are needed in a few areas, namely, the reduction of different metal salts within the membrane matrix, the structural morphology stability of affixing metal or metal oxides in graphene using laser irradiation and the possibility of achieving multifunctional membranes that can be used for water treatment. Such membranes can have photothermal and electrothermal properties for membrane distillation, photocatalytic effect for fouling mitigation and degradation of organic foulants, and ion-sensing surface for early detection of toxic heavy metal in feed.

4. Conclusion

As the use of localized heating to improve MD performance proliferates, the need to optimize membrane materials that can be used for such a purpose is required. In this study, one of such materials, the LIG Janus membranes, was studied. The effects of membrane pore structures, PDMS coating sequence and the addition of silver nanoparticles during the fabrication process on the performance of MD were assessed.

Results show that laser irradiation on the surface containing smaller pore features to create the LIG Janus membranes generally gave an improved flux performance of up to 53.6% and a decrease in specific energy of up to 35.4%. The coating sequence affected the MD performance in different ways depending on the membrane face that was treated. For the membrane face with smaller pores (i.e., shiny side), the PDMS coating carried out before laser irradiation to create the LIG Janus membranes (PDMS-BLSS) gave a flux improvement of up to 24.5% and

decrease in specific energy of up to 19.7%. On the other hand, for the membrane face with larger pores (i.e., dull side), coating the LIG before laser irradiation (PDMS-BLDS) resulted in a flux reduction of up to 20.8% and an increase in specific energy of up to 27.1%. This can be attributed to PDMS sealing the pores of the surface with smaller pore structures (i.e., shiny side) when they were being coated after laser irradiation, effectively reducing the porosity of the membrane. Despite being a photothermal material, undoped silver in the LIG Janus membranes did not yield synergistic results when operated in an MD system with simultaneous photo- and electro-thermal heating, as the summation of fluxes in the individual heating methods were higher than that of the flux obtained with simultaneous photo- and electro-thermal heating. However, the silver-doped Janus LIG membranes exhibited a synergistic effect when heated simultaneously with photo- and electro-thermal heating. Furthermore, the silver-doped Janus LIG membranes displayed advantageous photothermal heating properties, improving flux by 43.1–65.8% and decreasing specific energy by 15.2–30.5%, while maintaining similar electrothermal heating properties.

Overall, this study shows that that LIG Janus membranes can be optimized for simultaneous photo- and electro-thermal MD by reducing the size of the pore features on the surface being irradiated by the laser, coating it with the PDMS before irradiating the membrane with laser and embedding photothermal materials within the LIG matrix. The results here are expected to be valuable for paving the way for embedding different materials into the LIG membranes, which could leverage the vast functional materials that have emerged on doping of graphene.

CRediT authorship contribution statement

Yong Zen Tan: Writing – review & editing, Writing – original draft, Visualization, Validation, Investigation, Formal analysis, Data curation, Conceptualization. **Navin Raj Tamilselvam:** Methodology, Investigation, Formal analysis. **Nur Hashimah Alias:** Writing – review & editing, Visualization, Formal analysis. **Jia Zheng Oor:** Formal analysis. **Ronn Goei:** Validation, Formal analysis. **Alfred Iing Yoong Tok:** Validation, Formal analysis. **Jia Wei Chew:** Writing – review & editing, Supervision, Project administration, Funding acquisition.

Declaration of competing interest

The authors declare that they have no known competing financial interests or personal relationships that could have appeared to influence the work reported in this paper.

Data availability

Data will be made available on request.

Acknowledgements

This study was supported by A*STAR (Singapore) Advanced Manufacturing and Engineering (AME) under its Pharma Innovation Programme Singapore (PIPS) (A20B3a0070); A*STAR (Singapore) Advanced Manufacturing and Engineering (AME) under its Individual Research Grant (IRG) program (A2083c0049); the Singapore Ministry of Education Academic Research Tier 1 Grant (2019-T1-002-065; RG100/19) and the Singapore Ministry of Education Academic Research Tier 2 Grant (MOE-MOET2EP10120-0001). NHA would like to thank the Singapore National Academy of Science (SNAS) and National Research Foundation, Singapore (NRF) for the Singapore Academies South-East Asia Fellowship (SASEAF) awarded.

Appendix A. Supplementary data

Supplementary data to this article can be found online at https://doi.org/10.1016/j.memsci.2024.122900.

References

[1] M.A. Al-Ghouti, M.A. Al-Kaabi, M.Y. Ashfaq, D.A. Da'na, Produced water characteristics, treatment and reuse: a review, J. Water Process Eng. 28 (September 2018) (2019) 222–239, https://doi.org/10.1016/j.jwpe.2019.02.001.
[2] J.R. Stokes, A.X. Horvath, Energy and Air Emission Effects of Water Supply, ACS Publications, 2009.
[3] C. Skuse, A. Gallego-Schmid, A. Azapagic, P. Gorgojo, Can emerging membrane-based desalination technologies replace reverse osmosis? Desalination 500 (2021) 114844 https://doi.org/10.1016/j.desal.2020.114844.
[4] N. Dhakal, S.G. Salinas-Rodriguez, J. Hamdani, A. Abushaban, H. Sawalha, J. C. Schippers, M.D. Kennedy, Is desalination a solution to freshwater scarcity in developing countries? Membranes 12 (4) (2022) https://doi.org/10.3390/membranes12040381.
[5] E. Jones, M. Qadir, M.T.H. van Vliet, V. Smakhtin, S.-m. Kang, The state of desalination and brine production: a global outlook, Sci. Total Environ. 657 (2019) 1343–1356, https://doi.org/10.1016/j.scitotenv.2018.12.076.
[6] C. Kenigsberg, S. Abramovich, O. Hyams-Kaphzan, The effect of long-term brine discharge from desalination plants on benthic foraminifera, PLoS One 15 (1) (2020) e0227589, https://doi.org/10.1371/journal.pone.0227589.
[7] M.L. Cambridge, A. Zavala-Perez, G.R. Cawthray, J. Mondon, G.A. Kendrick, Effects of high salinity from desalination brine on growth, photosynthesis, water relations and osmolyte concentrations of seagrass Posidonia australis, Mar. Pollut. Bull. 115 (1) (2017) 252–260, https://doi.org/10.1016/j.marpolbul.2016.11.066.
[8] I. Sola, Y. Fernández-Torquemada, A. Forcada, C. Valle, Y. del Pilar-Ruso, J. M. González-Correa, J.L. Sánchez-Lizaso, Sustainable desalination: long-term monitoring of brine discharge in the marine environment, Mar. Pollut. Bull. 161 (2020) 111813, https://doi.org/10.1016/j.marpolbul.2020.111813.
[9] H. Frank, K.E. Fussmann, E. Rahav, E. Bar Zeev, Chronic effects of brine discharge from large-scale seawater reverse osmosis desalination facilities on benthic bacteria, Water Res. 151 (2019) 478–487, https://doi.org/10.1016/j.watres.2018.12.046.
[10] H. Frank, E. Rahav, E. Bar-Zeev, Short-term effects of SWRO desalination brine on benthic heterotrophic microbial communities, Desalination 417 (2017) 52–59, https://doi.org/10.1016/j.desal.2017.04.031.
[11] N. Voutchkov, Energy use for membrane seawater desalination – current status and trends, Desalination 431 (2018) 2–14, https://doi.org/10.1016/j.desal.2017.10.033.
[12] N. Thomas, M.O. Mavukkandy, S. Loutatidou, H.A. Arafat, Membrane distillation research & implementation: lessons from the past five decades, Separ. Purif. Technol. 189 (2017) 108–127, https://doi.org/10.1016/j.seppur.2017.07.069.
[13] A. Alkhudhiri, N. Darwish, N. Hilal, Membrane distillation: a comprehensive review, Desalination 287 (2012) 2–18, https://doi.org/10.1016/j.desal.2011.08.027.
[14] V. Belessiotis, S. Kalogirou, E. Delyannis, Chapter Four - Membrane Distillation, in: V. Belessiotis, S. Kalogirou, E. Delyannis (Eds.), Thermal Solar Desalination, Academic Press2016, pp. 191-251. https://doi.org/https://doi.org/10.1016/B978-0-12-809656-7.00004-0..
[15] A. Ali, C.A. Quist-Jensen, F. Macedonio, E. Drioli, Optimization of module length for continuous direct contact membrane distillation process, Chem. Eng. Process: Process Intensif. 110 (2016) 188–200, https://doi.org/10.1016/j.cep.2016.10.014.
[16] A. Anvari, A. Azimi Yancheshme, K.M. Kekre, A. Ronen, State-of-the-art methods for overcoming temperature polarization in membrane distillation process: a review, J. Membr. Sci. 616 (2020) 118413, https://doi.org/10.1016/j.memsci.2020.118413.
[17] Z. Chen, J. Li, J. Zhou, X. Chen, Photothermal Janus PPy-SiO2@PAN/F-SiO2@PVDF-HFP membrane for high-efficient, low energy and stable desalination through solar membrane distillation, Chem. Eng. J. 451 (2023), https://doi.org/10.1016/j.cej.2022.138473.
[18] Y. Qian, L. Chen, L. Zhu, Application of the electrical localized heating method in direct contact Membrane Distillation Crystallization process, Desalination 564 (2023), https://doi.org/10.1016/j.desal.2023.116770.
[19] F.E. Ahmed, B.S. Lalia, R. Hashaikeh, N. Hilal, Alternative heating techniques in membrane distillation: a review, Desalination 496 (2020) 114713, https://doi.org/10.1016/j.desal.2020.114713.
[20] Y. Wang, X. Liu, J. Ge, J. Li, Y. Jin, Distillation performance in a novel minichannel membrane distillation device, Chem. Eng. J. 462 (2023), https://doi.org/10.1016/j.cej.2023.142335.
[21] T. Eljaddi, C. Cabassud, Wetting of photoplasmonic PVDF/silver membranes in photothermal membrane distillation: identification of wetting mechanisms and comparison of wetting dynamics, Desalination 540 (2022) 116019, https://doi.org/10.1016/j.desal.2022.116019.
[22] H. Ye, X. Li, L. Deng, P. Li, T. Zhang, X. Wang, B.S. Hsiao, Silver nanoparticle-enabled photothermal nanofibrous membrane for light-driven membrane distillation, Ind. Eng. Chem. Res. 58 (8) (2019) 3269–3281, https://doi.org/10.1021/acs.iecr.8b04708.
[23] A. Alsaati, A.M. Marconnet, Energy efficient membrane distillation through localized heating, Desalination 442 (2018) 99–107, https://doi.org/10.1016/j.desal.2018.05.009.
[24] Y.Z. Tan, S.P. Chandrakant, J.S.T. Ang, H. Wang, J.W. Chew, Localized induction heating of metallic spacers for energy-efficient membrane distillation, J. Membr. Sci. 606 (2020) 118150, https://doi.org/10.1016/j.memsci.2020.118150.
[25] A. Anvari, A. Azimi Yancheshme, A. Ronen, Enhanced performance of membrane distillation using radio-frequency induction heated thermally conducting feed spacers, Separ. Purif. Technol. 250 (2020) 117276, https://doi.org/10.1016/j.seppur.2020.117276.

[26] A. Anvari, K.M. Kekre, A. Azimi Yancheshme, Y. Yao, A. Ronen, Membrane distillation of high salinity water by induction heated thermally conducting membranes, J. Membr. Sci. 589 (2019) 117253, https://doi.org/10.1016/j.memsci.2019.117253.
[27] S.T. M, P.T. Lin, Y.-H. Chiao, J. Widakdo, C.-H. Chuang, S.F. Rahmadhanty, S. Yoshikawa, W.-S. Hung, High performance self-heated membrane distillation system for energy efficient desalination process, J. Mater. Chem. A 9 (12) (2021) 7868–7880, https://doi.org/10.1039/D0TA11724B.
[28] J. Huang, T. Tang, Y. He, Coupling photothermal and Joule-heating conversion for self-heating membrane distillation enhancement, Appl. Therm. Eng. 199 (2021) 117557, https://doi.org/10.1016/j.applthermaleng.2021.117557.
[29] F.E. Ahmed, B.S. Lalia, R. Hashaikeh, N. Hilal, Enhanced performance of direct contact membrane distillation via selected electrothermal heating of membrane surface, J. Membr. Sci. 610 (2020) 118224, https://doi.org/10.1016/j.memsci.2020.118224.
[30] A.V. Dudchenko, C. Chen, A. Cardenas, J. Rolf, D. Jassby, Frequency-dependent stability of CNT Joule heaters in ionizable media and desalination processes, Nat. Nanotechnol. 12 (6) (2017) 557–563, https://doi.org/10.1038/nnano.2017.102. http://www.nature.com/nnano/journal/v12/n6/abs/nnano.2017.102.html#supplementary-information.
[31] M. Gao, C.K. Peh, F.L. Meng, G.W. Ho, Photothermal membrane distillation toward solar water production, Small Methods 5 (5) (2021) 2001200, https://doi.org/10.1002/smtd.202001200.
[32] A.H. Avci, S. Santoro, A. Politano, M. Propato, M. Micieli, M. Aquino, Z. Wenjuan, E. Curcio, Photothermal sweeping gas membrane distillation and reverse electrodialysis for light-to-heat-to-power conversion, Chemical Engineering and Processing - Process Intensification 164 (2021) 108382, https://doi.org/10.1016/j.cep.2021.108382.
[33] Y.Z. Tan, H. Wang, L. Han, M.B. Tanis-Kanbur, M.V. Pranav, J.W. Chew, Photothermal-enhanced and fouling-resistant membrane for solar-assisted membrane distillation, J. Membr. Sci. 565 (2018) 254–265, https://doi.org/10.1016/j.memsci.2018.08.032.
[34] A.G. Razaqpur, Y. Wang, X. Liao, Y. Liao, R. Wang, Progress of photothermal membrane distillation for decentralized desalination: a review, Water Res. 201 (2021) 117299, https://doi.org/10.1016/j.watres.2021.117299.
[35] J. Wu, K.R. Zodrow, P.B. Szemraj, Q. Li, Photothermal nanocomposite membranes for direct solar membrane distillation, J. Mater. Chem. A 5 (45) (2017) 23712–23719, https://doi.org/10.1039/C7TA04555G.
[36] Z. Wang, Z. Li, B. Yong, H. Huang, L. Yao, L. Deng, Depression of electro-oxidation of Ti3C2Tx MXene Joule heater by alternating current for Joule heating membrane distillation, Chem. Eng. J. 461 (2023), https://doi.org/10.1016/j.cej.2023.142149.
[37] Q. Kang, Y. Zhai, F. Zhao, L. Yang, Y. Yang, H.-D. Park, Z. Li, H. Chen, G. Sun, Salt-resistant and antibacterial polyvinyl alcohol/chitosan/silver-loaded graphene oxide electrospun nanofiber membrane for high-efficiency solar-driven desalination, Chem. Eng. Res. Des. 205 (2024) 107–117, https://doi.org/10.1016/j.cherd.2024.03.042.
[38] Y.Z. Tan, E.H. Ang, J.W. Chew, Metallic spacers to enhance membrane distillation, J. Membr. Sci. 572 (2019) 171–183, https://doi.org/10.1016/j.memsci.2018.10.073.
[39] E.H. Ang, Y.Z. Tan, J.W. Chew, A three-dimensional plasmonic spacer enables highly efficient solar-enhanced membrane distillation of seawater, J. Mater. Chem. A 7 (17) (2019) 10206–10211, https://doi.org/10.1039/C8TA11896E.
[40] A. Politano, P. Argurio, G. Di Profio, V. Sanna, A. Cupolillo, S. Chakraborty, H. A. Arafat, E. Curcio, Photothermal membrane distillation for seawater desalination, Adv. Mater. 29 (2) (2017) 1603504–n/a, https://doi.org/10.1002/adma.201603504.
[41] C. Cao, F. Liu, F. Li, O.R. Uzochukwu, L. Chen, A novel strategy for retarding membrane wetting under electrical field: embedding silver nanowires into UiO-66-NH2/graphene oxide composite thin membrane, Desalination 574 (2024) 117263, https://doi.org/10.1016/j.desal.2023.117263.
[42] X. Wu, G.Y. Chen, G. Owens, D. Chu, H. Xu, Photothermal materials: a key platform enabling highly efficient water evaporation driven by solar energy, Mater. Today Energy 12 (2019) 277–296, https://doi.org/10.1016/j.mtener.2019.02.001.
[43] V.-D. Dao, H.-S. Choi, Carbon-based sunlight absorbers in solar-driven steam generation devices, Global Challenges 2 (2) (2018) 1700094, https://doi.org/10.1002/gch2.201700094.
[44] N.S. Fuzil, N.H. Othman, N.H. Alias, F. Marpani, M.H.D. Othman, A.F. Ismail, W. J. Lau, K. Li, T.D. Kusworo, I. Ichinose, M.M.A. Shirazi, A review on photothermal material and its usage in the development of photothermal membrane for sustainable clean water production, Desalination 517 (2021) 115259, https://doi.org/10.1016/j.desal.2021.115259.
[45] X. Li, G. Ni, T. Cooper, N. Xu, J. Li, L. Zhou, X. Hu, B. Zhu, P. Yao, J. Zhu, Measuring conversion efficiency of solar vapor generation, Joule 3 (8) (2019) 1798–1803, https://doi.org/10.1016/j.joule.2019.06.009.
[46] E. Pop, V. Varshney, A.K. Roy, Thermal properties of graphene: fundamentals and applications, MRS Bull. 37 (12) (2012) 1273–1281, https://doi.org/10.1557/mrs.2012.203.
[47] B. Liu, K. Zhou, Recent progress on graphene-analogous 2D nanomaterials: properties, modeling and applications, Prog. Mater. Sci. 100 (2019) 99–169, https://doi.org/10.1016/j.pmatsci.2018.09.004.
[48] Y. Fu, J. Hansson, Y. Liu, S. Chen, A. Zehri, M.K. Samani, N. Wang, Y. Ni, Y. Zhang, Z.-B. Zhang, Q. Wang, M. Li, H. Lu, M. Sledzinska, C.M.S. Torres, S. Volz, A. A. Balandin, X. Xu, J. Liu, Graphene related materials for thermal management, 2D Mater. 7 (1) (2019) 012001, https://doi.org/10.1088/2053-1583/ab48d9.
[49] A. Boretti, S. Al-Zubaidy, M. Vaclavikova, M. Al-Abri, S. Castelletto, S. Mikhalovsky, Outlook for graphene-based desalination membranes, npj Clean Water 1 (1) (2018) 5, https://doi.org/10.1038/s41545-018-0004-z.
[50] X.J. Lee, B.Y.Z. Hiew, K.C. Lai, L.Y. Lee, S. Gan, S. Thangalazhy-Gopakumar, S. Rigby, Review on graphene and its derivatives: synthesis methods and potential industrial implementation, J. Taiwan Inst. Chem. Eng. 98 (2019) 163–180, https://doi.org/10.1016/j.jtice.2018.10.028.
[51] L. Wang, M. Liu, Y. Wu, H. Zheng, Asymmetrically superwetting Janus membrane constructed by laser-induced graphene (LIG) for on-demand oil–water separation and electrothermal anti-/de-icing, Chem. Eng. J. 488 (2024) 150862, https://doi.org/10.1016/j.cej.2024.150862.
[52] J. Guo, M. Zhao, C. Chen, F. Wang, Z. Chen, A laser-induced graphene-based electrochemical immunosensor for nucleic acid methylation detection, Analyst 149 (1) (2024) 137–147, https://doi.org/10.1039/D3AN01628E.
[53] N. Dixit, S.P. Singh, Laser-induced graphene (LIG) as a smart and sustainable material to restrain pandemics and endemics: a perspective, ACS Omega 7 (6) (2022) 5112–5130, https://doi.org/10.1021/acsomega.1c06093.
[54] M. Nazeri, M. Ghalamboran, G. Grau, Laser-induced graphene electrodes for organic electrochemical transistors (OECTs), Advanced Materials Technologies 8 (17) (2023) 2300188, https://doi.org/10.1002/admt.202300188.
[55] A.P. Nguyen, H.M. Do, R. Khan, C. Ryu, C.V. Tran, S.-M. Kim, J.B. In, Fabrication of Co- and P-doped laser-induced graphene for use in water splitting applications, ACS Appl. Energy Mater. (2024), https://doi.org/10.1021/acsaem.4c00116.
[56] A.K. Thakur, H. Mahbub, F.H. Nowrin, M. Malmali, Highly robust laser-induced graphene (LIG) ultrafiltration membrane with a stable microporous structure, ACS Appl. Mater. Interfaces 14 (41) (2022) 46884–46895, https://doi.org/10.1021/acsami.2c09563.
[57] M. Lamarche, M.T. Dang, J. Lefebvre, J.D. Wuest, S. Roorda, Limonene as a green solvent for depositing thin layers of molecular electronic materials with controlled interdiffusion, ACS Sustain. Chem. Eng. 5 (7) (2017) 5994–5998, https://doi.org/10.1021/acssuschemeng.7b00779.
[58] A.V. Dudchenko, C. Chen, A. Cardenas, J. Rolf, D. Jassby, Frequency-dependent stability of CNT Joule heaters in ionizable media and desalination processes, Nat. Nanotechnol. 12 (6) (2017) 557–563, https://doi.org/10.1038/nnano.2017.102.
[59] Y. Yu, Z. Zhou, G. Huang, H. Cheng, L. Han, S. Zhao, Y. Chen, F. Meng, Purifying water with silver nanoparticles (AgNPs)-incorporated membranes: recent advancements and critical challenges, Water Res. 222 (2022) 118901, https://doi.org/10.1016/j.watres.2022.118901.
[60] J.-H. Li, X.-S. Shao, Q. Zhou, M.-Z. Li, Q.-Q. Zhang, The double effects of silver nanoparticles on the PVDF membrane: surface hydrophilicity and antifouling performance, Appl. Surf. Sci. 265 (2013) 663–670, https://doi.org/10.1016/j.apsusc.2012.11.072.
[61] M. Khayet, A. Velázquez, J.I. Mengual, Modelling mass transport through a porous partition, Effect of pore size distribution 29 (3) (2004) 279–299, https://doi.org/10.1515/JNETDY.2004.055.
[62] J. Liu, M. Liu, H. Guo, W. Zhang, K. Xu, B. Li, Mass transfer in hollow fiber vacuum membrane distillation process based on membrane structure, J. Membr. Sci. 532 (2017) 115–123. %@ 0376-7388.
[63] Ó. Andrjesdóttir, C.L. Ong, M. Nabavi, S. Paredes, A.S.G. Khalil, B. Michel, D. Poulikakos, An experimentally optimized model for heat and mass transfer in direct contact membrane distillation, Int. J. Heat Mass Tran. 66 (2013) 855–867. %@ 0017-9310.
[64] M. Qtaishat, T. Matsuura, B. Kruczek, M. Khayet, Heat and mass transfer analysis in direct contact membrane distillation, Desalination 219 (1–3) (2008) 272–292. %@ 0011-9164.
[65] E.F. Sheka, Y.A. Golubev, N.A. Popova, Graphene domain signature of Raman spectra of sp(2) amorphous carbons, Nanomaterials 10 (10) (2020) 2021, https://doi.org/10.3390/nano10102021.
[66] S.J. Goldie, S. Bush, J.A. Cumming, K.S. Coleman, A statistical approach to Raman analysis of graphene-related materials: implications for quality control, ACS Appl. Nano Mater. 3 (11) (2020) 11229–11239, https://doi.org/10.1021/acsanm.0c02361.
[67] R. Rodgers, G. Hill, Equations for vapour pressure versus temperature: derivation and use of the antoine equation on A hand-held programmable calculator, Br. J. Anaesth. 50 (5) (1978) 415–424, https://doi.org/10.1093/bja/50.5.415.
[68] Y.Z. Tan, M.S.R.S. Kapavarapu, J.Z. Oor, C.S. Ong, J.W. Chew, Laser-induced graphene Janus membrane for electrothermal membrane distillation, Desalination 540 (2022), 115994 %@ 0011-9164.